Solutions for Transients in Arbitrarily Branching Cables: I. Voltage Recording with a Somatic Shunt

Guy Major, Jonathan D. Evans, and J. Julian B. Jack
University Laboratory of Physiology, Oxford, OX1 3PT, United Kingdom

ABSTRACT An analytical solution is derived for voltage transients in an arbitrarily branching passive cable neurone model with a soma and somatic shunt. The response to injected currents can be represented as an infinite series of exponentially decaying components with different time constants and amplitudes. The time constants of a given model, obtained from the roots of a recursive transcendental equation, are independent of the stimulating and recording positions. Each amplitude is the product of three factors dependent on the corresponding root: one constant over the cell, one varying with the input site, and one with the recording site. The amplitudes are not altered by interchanging these sites. The solution reveals explicitly some of the parameter dependencies of the responses. An efficient recursive root-finding algorithm is described. Certain regular geometries lead to "lost" roots; difficulties associated with these can be avoided by making small changes to the lengths of affected segments. Complicated cells, such as a CA1 pyramid, produce many closely spaced time constants in the range of interest. Models with large somatic shunts and dendrites of unequal electrotonic lengths can produce large amplitude waveform components with surprisingly slow time constants. This analytic solution should complement existing passive neurone modeling techniques.

LIST OF SYMBOLS*

a	parameter of "alpha" function ([time-to-peak]$^{-1}$) [ms^{-1}] (Eq. 47)
a_j	surface area of jth segment $= \pi l_j d_j$ [μm^2]
a_s	surface area of soma $= \pi d_s^2$ [μm^2]
A_n	nth amplitude component of voltage response to *unit* point charge [mV] (Eq. 1)
$A_{n_{er}}$	A_n between segments e and r or vice versa (specify Z_e, X_r) [mV] (Eq. 33)
$\bar{A}_c$	constant in $\bar{G}_r(X_r, Z_e, p)$ for "mainline" segment c (Eq. 69)
$\bar{A}_s$	constant in $\bar{G}_r(X_r, Z_e, p)$ at soma (Eq. 78)
A'_c	$\bar{A}_c$ when $q = iw$ (Eq. 97)
A'_s	$\bar{A}_s$ when $q = iw$ (Eq. 95)
$\bar{B}_c$	constant in $\bar{G}_r(X_r, Z_e, p)$ for "mainline" segment c (Eq. 76)
$\bar{B}_e$	constant in $\bar{G}_r(X_r, Z_e, p)$ for stimulated segment e (Eq. 74)
B'_c	$\bar{B}_c$ when $q = iw$ (Eq. 98)
B'_e	$\bar{B}_e$ when $q = iw$ (Eq. 99)
c_{m_j}	capacitance per unit length of segment j ($= \pi d_j C_m$) [μF cm^{-1}]
c_s	lumped soma capacitance ($= \pi d_s^2 C_m$) [pF]
C_j	constant in y_j (Eq. 14)
C_s	corresponding constant at the soma (Eq. 17)
C_m	specific membrane capacitance [μFcm^{-2}]
$\bar{C}$	constant in $\bar{G}_r(X_r, Z_e, p)$ for recording sites distal to stimulus site (Eq. 71)
C'	$\bar{C}$ when $q = iw$ (Eq. 101)
d_j	diameter of segment j (subscript s means soma) [μm]
$dtrs_p$	the set of daughter segments of segment p
D_n	generalised Fourier coefficient of ψ_{jn} (Eq. 25)
E_n	position-independent "Electrical" part of A_n [mV] (Eq. 34)
g_{∞_j}	input conductance of segment j's infinite extension ($= [r_{m_j} r_{a_j}]^{-1/2}$) [nS] (Eq. 40)
g_s	total soma conductance, including shunt ($= g_{shunt} + g_{sm}$) [nS]
g_{sm}	soma membrane conductance ($= \pi d_s^2 / R_m$) ([nS]
g_{shunt}	somatic shunt conductance [nS]
$G_r(X_r, Z_e, t)$	voltage response at X_r to unit point charge at Z_e [mV] (Appendix 1)
$\bar{G}_r(X_r, Z_e, p)$	Laplace transform of $G_r(X_r, Z_e, t)$ with respect to p (Eqs. 57, 67, 68, 70, 72)
$G_s(Z_e, t)$	voltage response at soma to unit point charge at Z_e [mV] (Appendix 1)
$\bar{G}_s(Z_e, p)$	Laplace transform of $G_s(Z_e, t)$ with respect to p (Eqs. 57, 67)
H_{er}	lumped amplitude term for smooth inputs [mV] (Eqs. 93, 103, 104, 108)
$i(t)$	input current [nA] (Eqs. 47, 49, 51)
l_j	physical length of a segment j [μm]
L_{eff_j}	effective combined L of segment j and daughters [dimensionless] (Eq. 114)
L_j	electrotonic length ($= l_j/\lambda_j$) of segment j [dimensionless]
p	complex Laplace transform variable [dimensionless] (Eq. 57)
q	$\sqrt{1 + \tau_m p}$ [dimensionless] (Appendices 1 and 2)
Q	total input charge [pC]
r_{a_j}	axial resistance per unit length of segment j ($= 4R_i/\pi d_j^2$) [Ωcm^{-1}]
r_{m_j}	membrane resistance of a unit length of segment j ($= R_m/\pi d_j$) [Ωcm]
R_{er}	steady-state resistance between segments e and r (specify z_e and x_r) [MΩ] (Eq. 110)
R_i	axial resistivity [Ωcm]
R_m	specific membrane resistivity [Ωcm^2]
R_{shunt}	somatic shunt resistance ($= g_{shunt}^{-1}$) [MΩ]

Received for publication 22 October 1992 and in final form 26 February 1993.

Address reprint requests to G. Major at the University Laboratory of Physiology, Parks Rd., Oxford, OX1 3PT, United Kingdom. Tel.: 44-865-272507; Fax: 44-865-272469; e-mail: gm @ uk.ac.oxford.physiology.

0006-3495/93/07/423/27 $2.00

segs	the set of all segment indices j
stems	the set of indices of segments st originating from soma (i.e., stem segments)
t	time [ms]
$v_j(x_j, t)$	transmembrane voltage relative to resting potential, in segment j [mV]
$V_j(X_j, t)$	$v_j(x_j, t)$ with dimensionless space parameters [mV] (Eq. 2)
$\bar{V}_r(X_r, Z_e, p)$	Laplace transform of $V_j(X_j, t)$, recording in segment r, stimulating at Z_e
$\hat{v}_r(x_r, z_e)$	steady-state voltage at x_r given input at z_e [mV] (Eq. 110)
$v_s(t)$	transmembrane voltage relative to resting potential, at soma [mV]
$V_s(t)$	$V_j(t)$ at soma [mV]
w	q/i or $\sqrt{\tau_m/\tau_{sy_n} - 1}$, used when $\tau_{sy_n} < \tau_m$ [dimensionless] (Appendix 2)
x_j	physical distance from proximal end of segment j [μm]
X_j	electrotonic distance from proximal end of segment j ($= x_j/\lambda_j$) [dimensionless]
y_i	spatial part of (Eq. 13), in segment j
z_e	physical distance of excitation site from proximal end of segment e [μm]
Z_e	electrotonic distance of input site from proximal end of segment e [dimensionless]
	Greek symbols
α^2	separation constant (Eq. 13)
α_n	nth eigenvalue of boundary problem; satisfies (Eq. 22)
ϵ	somatic shunt parameter τ_s/τ_m [dimensionless]
Θ_n	$[1 - \epsilon(1 + \alpha_n^2)]/\alpha_n^2$ (Eq. 35)
κ_{jn}	nth voltage continuity normalisation factor of segment j (Eq. 31)
$\bar{\kappa}_j$	continuity factor in $\bar{G}_r$ for segment j (Eq. 66)
λ_j	space constant ($= (r_{m_j}/r_{a_j})^{1/2}$) of segment j [μm]
μ_j	branching constant of segment j; depends on α (Eq. 19)
μ_{jn}	μ_j when $\alpha = \alpha_n$
$\bar{\mu}_j$	branching constant in segment j for $\bar{G}_r$; depends on q (Eq. 64)
ψ_{jn}	spatial eigenfunction in segment j [dimensionless] (Eq. 26)
τ_{eff}	apparent τ_0 of a waveform by linear regression over specified interval [ms] (Eq. 55)
τ_m	time constant of dendritic membrane ($= R_m C_m = r_{m_j} c_{m_j}$) [ms]
τ_n	nth equalizing time constant [ms] (Eq. 1)
τ_s	effective time constant of soma with shunt included ($= c_s/g_s$) [ms]
τ_{sy}	synaptic time constant for single exponential current input [ms] (Eq. 49)
τ_{sy_n}	nth synaptic time constant for multiexponential current input [ms] (Eq. 51)

* Convenient units and relevant equation numbers in brackets and parentheses, respectively.

INTRODUCTION

Despite the mounting evidence for active conductances in dendrites (e.g., Ref. 1), *passive* cable modeling still has an important role to play as the foundation of our understanding of the function of dendritic trees. To construct a realistic model of a single neurone, it is necessary first to characterize its passive (voltage-independent) electrical properties, and then to overlay the correct mixture of active conductances. In what follows, we consider passive behavior only.

A passive cable model is a linear system. Its voltage response to an instantaneous *unit* point charge input (unit impulse) can be used to predict its response to an arbitrary input (e.g., Ref. 2, Chapter 13). In general, the unit impulse response of a passive neurone model will be a series of exponentially decaying components each with a different time constant τ_n and amplitude A_n (e.g., Ref. 3), of the form

$$v(t) = \sum_{n=0}^{\infty} A_n e^{-t/\tau_n}. \quad (1)$$

Knowledge of these amplitudes and time constants can provide useful insights into the behavior of a model as a range of possible parameters is explored (see below, also Ref. 4).

It is useful to be able to model a real neurone with complex morphology which has been impaled by a microelectrode. The possibility of a leak around the electrode (5) and of additional injury-induced conductances (6) requires an extra "shunt" conductance (7) to be included at the impalement site (usually the soma), lowering the effective membrane resistivity there. The effective membrane resistivity of the soma may also be lower than that in the dendrites for other reasons, e.g., because of tonic inhibitory conductances, or because of the presence of a higher density of ion channels in the somatic membrane. With the advent of whole-cell recording from neurones (e.g., Ref. 8), it is also useful to be able to model the opposite situation, where wash-out of cytoplasmic constituents has lead to the somatic membrane resistivity being *higher* than that of the dendrites (e.g., Ref. 9).

Analytical solutions for transients are known for the multicylinder model (4, Appendix A) and the multicylinder, soma + shunt model (10). A solution for *early* times for arbitrarily branching geometry has been described by Abbott et al. (11, 12, 81), based on the method of "trips"/images. For good accuracy, this solution requires a large number of terms at later times (12, 81): even relatively simple geometries composed of 10–20 segments need tens of thousands of terms.[1]

Exact solutions for arbitrarily branching geometry at *late* times have not been found, as far as we know. In such cases, modelers have resorted to techniques based on *numerical* approximations. The most commonly used method, and the most versatile, is compartmental modeling (e.g., Refs. 13–20). Another approach is the segmental cable method (e.g.,

[1] The number of terms seems to grow exponentially with the number of segments or, more precisely, with the number of possible "trips" between stimulation and recording site that are shorter than about $k\sqrt{T}$, where T is the time in units of membrane time constants, and k is a constant, usually ≥ 4 (G. Major, preliminary observations).

Refs. 21–24). Most versions of these techniques suffer from the disadvantage that they allow the production of a waveform only, and give no direct information about the underlying time constants and amplitudes. An exception is the matrix eigenfunction expansion method first outlined by Perkel et al. (25) and used more recently by Holmes et al. (26, 27). This compartmental approach gives approximations to the first n time constants and amplitudes, where n is the number of compartments in the model.

An *analytic* solution of the form (1) for models with a soma, arbitrarily branching geometry and a somatic shunt, would provide: (i) verification of results obtained by the approximate methods above, (ii) potentially more efficient and more accurate simulations, (iii) *explicit*, accurate values for the time constants and amplitudes making up waveforms, and (iv) insight into their parameter dependencies.

The *apparent* time constants and amplitudes extracted from model waveforms by "peeling" (e.g., Ref. 3), iterative exponential fitting or more "exotic" methods (e.g., DISCRETE (28), and other Transform-based algorithms) could be compared with the correct values. The reliability and consequences of model parameters deduced *indirectly* from fit-derived amplitudes and time constants (e.g., Refs. 4, 26, 27) could be further assessed and compared with the results of *direct* fitting (see below).

In this paper, following Rall (13), Durand (29), Kawato (30), Bluman and Tuckwell (31), and Evans et al. (10), such a solution is derived for impulse responses, using voltage continuity, current conservation, separation of variables, Laplace transforms, and complex residues (see Appendix 1 for derivation of amplitudes). The amplitude terms can also be derived using a modified orthogonality relation (32) (proofs supplied on request).

Standard extensions to the solution are stated for responses to some other commonly used input functions. The relationship of the solution to existing passive modeling techniques is discussed. Examples are given to illustrate the uses of the analytical solution, and to underline some important practical points about simplified representations, reciprocity relations, the difficulties associated with attempting to extract exponential components from experimental data, and "slow bends" (slowly changing apparent time constants). The latter can be used to constrain the fit nonuniqueness (33, 34) which is frequently encountered when attempting to match model responses to experimental data (20, 27, 35).

Some problems associated with certain special cases are discussed in Appendix 4. Solutions for perfect and imperfect somatic voltage clamp are given in the next paper (36), referred to as "II" below. Further applications of the solutions, with an emphasis on the problems of voltage clamping dendritic neurones, are given in the third paper of this series (37), referred to as "III" below.

GLOSSARY AND CONVENTIONS

To improve clarity, conventions have been adopted for indices appearing as subscripts. These are given in Table 1 and are adhered to throughout this paper. When double indexing is used, the segment index usually precedes the eigenvalue index.

TABLE 1 Index conventions

Eigenvalue and eigenfunction index	
n	(= 0, 1, 2, . . .), never used as a segment index
N	index n of fastest time constant included in waveform
Segment indices	
j	arbitrary
p	parent
d	daughter
r	segment recorded from
e	segment stimulated (excited)
c	segment in a chain
s	soma
st	stem segment
Set notation	
$d \in dtrs_p$	over all the daughters d of segment p
$st \in stems$	over all the stem segments st
$j \in segs$	over all segments j
$c \in chain_j$	over all segments in direct chain between soma and j (inclusive)
$\forall st \in stems$	for all stem segments st
$\mathcal{P}(j)$	the parent of segment j

See above for an alphabetic list of symbols reappearing more than a few paragraphs away from their definitions. Convenient units are given in *square brackets*, and are used throughout this paper. Relevant equation numbers or definitions are given in parentheses. To help the reader, several symbols sound similar to their semantics, for example: ψ ("psi") for "spatial eigenfunction," κ for "continuity factor," p for "parent."

Key equations appear in *boxes*. Citations are given in parentheses, and equations are referred to in the text as "Eq. X."

UNIT IMPULSE RESPONSE

Definition of the system

Consider a model neurone consisting of a soma with a shunt and one or more dendritic trees, each composed of a number of branching cylindrical segments. Each segment is identified by an index j (any convenient numbering scheme could be adopted; for example a left-first, depth-first traversal of the dendritic trees with j going from 1 to the total number of segments). In Fig. 1 this is illustrated using part of the hippocampal CA1 pyramidal neurone used below in Example 1. Each segment j has physical length l_j and diameter d_j. The branching pattern can be coded using set notation: each nonterminal (or parent) segment (with index p) is assigned a set $dtrs_p$, whose elements are the segment indices d of its daughters (those segments originating from its distal end). Segments originating from the soma are called "stem" segments, and their indices st are the elements of the set *stems*. Summations (Σ) and products (Π) are over *every* member of the relevant set.

At time $t = 0$, a unit point *charge* is injected at a distance z_e (moving away from the soma) along the stimulated ("excited") segment e, and the transient voltage response $v_r(x_r, z_e, t)$ is recorded at a distance x_r along segment r. Distance along an arbitrary segment j is denoted by x_j. It is convenient to use the dimensionless electrotonic distances, e.g., $X_r = x_r/\lambda_r$ and $Z_e = z_e/\lambda_e$ (where λ_j is the space constant

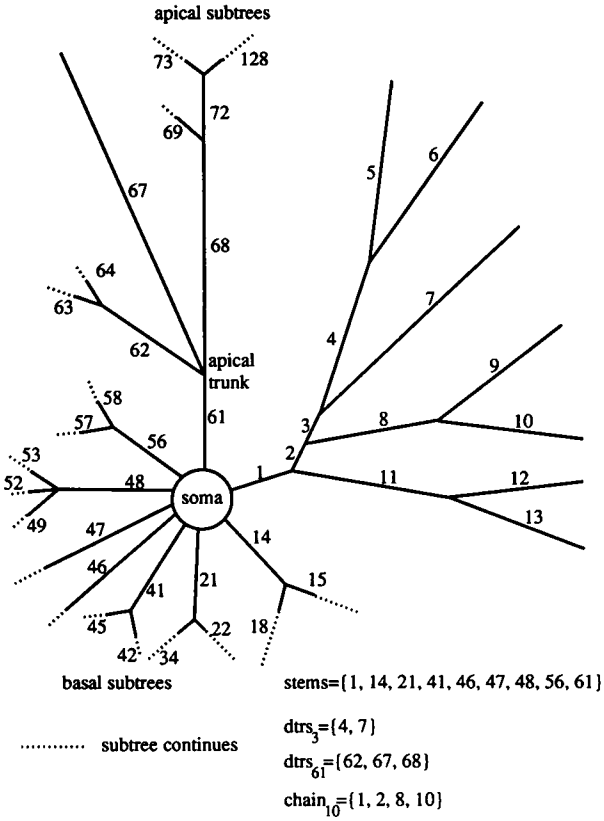

FIGURE 1 Illustration of indexing conventions: branching diagram of *part* of the dendritic arbor of the hippocampal CA1 pyramidal cell in Example 1. The scheme for numbering j, the segment index, is a left-first, depth-first traversal of the tree. Where there is a jump in the numbering, there is also a dotted line indicating the presence of a subtree which has not been drawn in full. Some examples are given of the set notation adopted here, for instance, $chain_{10}$, the set of segments on a mainline chain from soma to segment 10, consists of segments 1, 2, 8, and 10, and $dtrs_{61}$, the set of daughters of segment 61, consists of segments 62, 67, and 68. See Fig. 2 for representations of the entire dendritic arbor.

of segment j: see List of Symbols). Note that dimensional units are used for time.[2]

Define

$$V_r(X_r, Z_e, t) \equiv v_r(x_r, z_e, t). \tag{2}$$

To obtain $V_r(X_r, Z_e, t)$, it is necessary to solve, for each segment j, the *cable equation*

$$\frac{\partial^2 V_j}{\partial X_j^2} - \tau_m \frac{\partial V_j}{\partial t} - V_j = 0, \tag{3}$$

where τ_m is the dendritic membrane time constant, with *boundary conditions* as follows.

(i) At terminations:

$$\left(\frac{\partial V_j}{\partial X_j}\right)_{X_j = L_j} = 0 \tag{4}$$

(sealed ends, i.e., no axial current flow).

(ii) At branch points:

In segment j, axial current is given by

$$I_{a_j} = -\frac{1}{r_{a_j}\lambda_j}\frac{\partial V_j}{\partial X_j}, \tag{5}$$

where r_{a_j} is the axial resistance per unit length.

Axial current at a branch point is conserved, so

$$\frac{1}{r_{a_p}\lambda_p}\left(\frac{\partial V_p}{\partial X_p}\right)_{X_p = L_p} = \sum_{d \in dtrs_p} \frac{1}{r_{a_d}\lambda_d}\left(\frac{\partial V_d}{\partial X_d}\right)_{X_d = 0}, \tag{6}$$

where $d \in dtrs_p$ means the summation is over all the daughter segments d of segment p. Since $g_{\infty_j} = (r_{a_j}\lambda_j)^{-1}$ (e.g., Ref. 13, p. 63), it follows that

$$g_{\infty_p}\left(\frac{\partial V_p}{\partial X_p}\right)_{X_p = L_p} = \sum_{d \in dtrs_p} g_{\infty_d}\left(\frac{\partial V_d}{\partial X_d}\right)_{X_d = 0}. \tag{7}$$

(iii) At the soma:

The current flowing *out* through the soma is the sum of the currents *leaving* the stem dendrites: combining Eqs. 5–7 in Ref. 29 and Eq. 24 in Ref. 3 gives

$$g_s\left(V_s + \epsilon\tau_m \frac{\partial V_s}{\partial t}\right) = \sum_{st \in stems} g_{\infty_{st}}\left(\frac{\partial V_{st}}{\partial X_{st}}\right)_{X_{st} = 0}, \tag{8}$$

where $st \in stems$ means the summation is over all the stem segments st, V_s is the voltage at the soma, $g_s = g_{sm} + g_{shunt}$ is the total somatic conductance (g_{sm} is the soma membrane conductance, assuming uniform R_m, and g_{shunt} is the somatic shunt conductance) and $\epsilon = \tau_s/\tau_m = g_{sm}/g_s$ = effective somatic R_m/dendritic R_m is the somatic shunt parameter (see List of Symbols). Values of ϵ greater than one (equivalent to small negative shunts of magnitude $\leq g_{sm}$) correspond to situations where, perhaps because of "wash-out," the soma membrane has a lower conductance per unit area than that of the dendrites.

(iv) Voltage continuity constraints:

$$V_p(L_p) = V_d(0) \text{ at branch points, } \forall d \in dtrs_p, \tag{9}$$

(i.e. for all daughters of p),

$$V_{st}(0) = V_s \text{ at soma, } \forall st \in stems \tag{10}$$

(i.e. for all stem segments st).

The unit point charge input gives the voltage delta function

[2] This has several (debatable) justifications: (i) the derivation of responses to more general inputs is slightly more convenient; (ii) when there is a shunt, the slowest time constant τ_0 is no longer equal to the dendritic membrane time constant τ_m, which is now different from the effective soma membrane time constant τ_s; (iii) it is slightly more convenient to generalize the solution to models with nonuniform τ_m.

(impulse) *initial condition*

$$V_j(X_j, Z_e, 0) = \begin{cases} (\tau_m g_{\infty_e})^{-1}\delta(X_e - Z_e) & \text{if } j = e \\ 0 & \text{otherwise,} \end{cases} \quad (11)$$

since the capacitance per space constant of segment j is

$$c_{m_j}\lambda_j = \frac{\tau_m}{r_{m_j}}\lambda_j = \frac{\tau_m}{(r_{m_j}r_{a_j})^{1/2}} = \tau_m g_{\infty_j}, \quad (12)$$

where for segment j, c_{m_j} is the membrane capacitance per unit length, and r_{m_j} is the membrane resistance of a unit length.

The system to be solved is then defined by Eqs. 3–11.

Separation of variables solution

It is easily shown (e.g., Ref. 3) that a general solution of Eq. 3 in separable form, with α^2 as the separation constant, is

$$V_j(X_j, t) = y_j(X_j)e^{-(1+\alpha^2)t/\tau_m}, \quad (13)$$

where $y_j(X_j)$, the spatial part of the solution, is given by

$$y_j(X_j) = C_j[\cos\alpha(L_j - X_j) + \mu_j \sin\alpha(L_j - X_j)] \quad (14)$$

and C_j and μ_j are arbitrary constants. At $X_j = L_j$, y_j reduces simply to C_j. The ratio of the values of y_j at the two ends of the segment can be expressed as

$$y_j(0)/y_j(L_j) = \cos\alpha L_j + \mu_j \sin\alpha L_j. \quad (15)$$

This represents an important basic relation for each segment, and underlies the normalization factors κ_{jn} introduced below in Eq. 25.

Application of boundary conditions

Applying the continuity constraint (Eq. 9) to Eqs. 13 and 14 at a branch point where $X_p = L_p$ (end of parent segment) and $X_d = 0$ for all the daughters d, gives

$$C_p = C_d(\cos\alpha L_d + \mu_d \sin\alpha L_d), \quad (16)$$

which holds true for *all* the daughter segments d. Applying the voltage continuity constraint at the soma gives

$$C_s = y_{st}(0) = C_{st}(\cos\alpha L_{st} + \mu_{st}\sin\alpha L_{st}) \quad \forall st \in stems, \quad (17)$$

where C_s is an arbitrary constant. Different daughter segments (or stem segments) can in general have different values of C_d, L_d, and μ_d.

Using Eqs. 13 and 14 in boundary condition (Eq. 7) gives

$$-g_{\infty_p}\alpha\mu_p C_p = \sum_{d\in dtrs_p} g_{\infty_d}\alpha C_d(\sin\alpha L_d - \mu_d\cos\alpha L_d), \quad (18)$$

which on using Eq. 16 and simplifying gives

$$\mu_p = -\frac{1}{g_{\infty_p}}\left\{\sum_{d\in dtrs_p} g_{\infty_d}\left(\frac{1 - \mu_d\cot\alpha L_d}{\cot\alpha L_d + \mu_d}\right)\right\}. \quad (19)$$

Note that if $\alpha = 0$, $\mu_p = 0$ also. Singularities (points at which the value is undefined) occur in μ_p whenever $(\cot\alpha L_d + \mu_d) = 0$ for one of the daughter segments d. Special cases occur when two or more such singularities from different daughters coincide at the same value of α (see Appendix 4), or when a singularity in $\cot\alpha L_d$ coincides with a singularity in μ_d.

Boundary condition (Eq. 4) gives

$$\mu_j = 0, \quad \text{(for terminal segments).} \quad (20)$$

Thus, after application of the voltage continuity and current conservation constraints, together with the terminal boundary condition, μ_j for a given segment j is defined *recursively* by Eqs. 19 and 20, and its value depends on α.

Recursive transcendental equation for the eigenvalues

Use of Eqs. 13 and 14 in the somatic boundary condition (Eq. 8) gives

$$C_s g_s[1 - \epsilon(1 + \alpha^2)]e^{-(1+\alpha^2)t/\tau_m} = \sum_{st\in stems} g_{\infty_{st}}C_{st}\alpha[\sin\alpha L_{st} - \mu_{st}\cos\alpha L_{st}]e^{-(1+\alpha^2)t/\tau_m}, \quad (21)$$

which may be simplified using Eq. 17 to

$$g_s\frac{[1 - \epsilon(1 + \alpha^2)]}{\alpha} = \sum_{st\in stems} g_{\infty_{st}}\left(\frac{1 - \mu_{st}\cot\alpha L_{st}}{\cot\alpha L_{st} + \mu_{st}}\right). \quad (22)$$

This *recursive transcendental equation* must be solved for values of $\alpha \geq 0$ to give the eigenvalues α_n, $n = 0, 1, 2, \ldots$, which satisfy the boundary conditions and other model parameters (see Implementation section for details of a root-finding algorithm, and see Fig. 5 for a plot of an example transcendental function). There is an analogy between Equations 19 and 22, and the recursive algorithm introduced by Rall (38) for the calculation of steady state input conductance in trees with arbitrary branching (also see Appendices 1 and 3). Both methods exploit voltage continuity and current conservation at branch points.

For a model composed only of unbranched cylinders originating from the soma (10), Eq. 22 becomes

$$g_s\frac{[1 - \epsilon(1 + \alpha^2)]}{\alpha} = \sum_{j\in segs} g_{\infty_j}\tan\alpha L_j. \quad (23)$$

To make clearer their dependencies on g_{shunt} and g_{sm}, the left-hand sides of Equations 22 and 23 can be written as $g_{shunt}/\alpha - g_{sm}\alpha$ (since $g_s\epsilon = g_s(c_s/g_s)/(c_s/g_{sm}) = g_{sm}$).

Time constants

Comparing Eqs. 1 and 13, it can be seen that each α_n corresponds to a time constant τ_n, where

$$\tau_n = \tau_m/(1 + \alpha_n^2), \tag{24}$$

(Equation 22 in Ref. 3.)

Continuous spatial eigenfunctions

When $\alpha = \alpha_n$, define C_{jn} to be the value of C_j and μ_{jn} to be the value of μ_j, for segment j. The spatial part $y_j(X_j)$ of the separable solution (Eq. 13) may then be expressed, for $\alpha = \alpha_n$, in a more convenient form by writing

$$C_{jn} = D_n\kappa_{jn}, \tag{25}$$

where the coefficient D_n is independent of the segment, and κ_{jn} is a normalization factor (for the jth segment and the nth eigenvalue), ensuring voltage continuity at branch points. Thus for segment j, a spatial eigenfunction ψ_{jn} can be defined with associated eigenvalue α_n, by

$$\psi_{jn}(X_j) = \kappa_{jn}[\cos\alpha_n(L_j - X_j) + \mu_{jn}\sin\alpha_n(L_j - X_j)], \tag{26}$$

so that when $\alpha = \alpha_n$,

$$y_j(X_j) = D_n\psi_{jn}(X_j). \tag{27}$$

We note that the eigenvalues α_n are implicitly involved in the boundary conditions, and therefore their associated eigenfunctions ψ_{jn} will be nonorthogonal (32).

The continuity factors κ_{jn}, using Eqs. 25 and 16, satisfy

$$\kappa_{dn} = \frac{\kappa_{pn}}{(\cos\alpha_nL_d + \mu_{dn}\sin\alpha_nL_d)}, \tag{28}$$

where p is a parent segment and d is one of its daughters. In order to satisfy the constraint (Eq. 10) and to ensure voltage continuity at the soma, we take

$$\psi_{stn}(0) = 1 \qquad \forall st \in stems, \tag{29}$$

and thus it follows that

$$\kappa_{stn} = \frac{1}{(\cos\alpha_nL_{st} + \mu_{stn}\sin\alpha_nL_{st})} \qquad \forall st \in stems. \tag{30}$$

Combining Eqs. 28 and 30, gives the iterative definition

$$\kappa_{jn} = \prod_{c\in chain_j} (\cos\alpha_nL_c + \mu_{cn}\sin\alpha_nL_c)^{-1}, \tag{31}$$

where the elements of $chain_j$ are the indices of every segment c in a "chain of direct descent" ("mainline"), starting from the stem segment of the tree containing j, and ending with segment j itself. In other words, κ_{jn} is the ratio of ψ_{jn} at the distal end of segment j to ψ_n at the soma. Note that if $\alpha_0 = 0$ (no shunt case), then $\kappa_{j0} = 1$, and $\psi_{j0} = 1$ throughout the cell, corresponding to a uniform distribution of charge.

Amplitudes

By linear superposition of the solutions of the form (Eq. 13), using Eqs. 24, 25, and 27, the general solution to the cell's voltage response can be written as

$$V_r(X_r, Z_e, t) = \sum_{n=0}^{\infty} D_n\psi_{rn}(X_r)e^{-t/\tau_n}. \tag{32}$$

Since $A_n = D_n\psi_{rn}$ (compare Eq. 1 with 32), it can be shown using techniques from complex analysis (see Appendix 1) that, for an impulse of unit charge, injected into the "excited" segment e and recording from segment r:

$$A_{n_{er}} \equiv A_n = E_n\psi_{en}(Z_e)\psi_{rn}(X_r), \tag{33}$$

where the position-independent ("Electrical") component is given (except when $n = 0$ in the no-shunt case) by

$$E_n \equiv \frac{2}{\tau_m[g_s(2\epsilon + \theta_n) + \sum_{j\in segs} g_{\infty_j}\kappa_{jn}^2(1 + \mu_{jn}^2)L_j]}, \tag{34}$$

and the spatial eigenfunction $\psi_{jn}(X_j)$ is defined in Eq. 26, κ_{jn}, the continuity factor, in Eq. 31, and

$$\theta_n \equiv \frac{1 - \epsilon(1 + \alpha_n^2)}{\alpha_n^2}. \tag{35}$$

To make clearer its dependence on g_{shunt} and g_{sm}, the term $g_s(2\epsilon + \theta_n)$ can be written $g_{sm} + g_{shunt}/\alpha_n^2$. Note the *symmetry between the stimulation and the recording sites* in Eq. 33: interchanging them will have no effect upon the resulting voltage transient. With both stimulation and recording site at the soma, $A_{n_{ss}} \equiv A_n = E_n$.

If $\alpha_0 = 0$ (case where $\epsilon = 1$), it can be shown that A_0 can be written

$$A_{0_{er}} = \frac{1}{\tau_m[g_s + \sum_{j\in segs} g_{\infty_j}L_j]}, \tag{36}$$

which is the same as (total capacitance)$^{-1}$.

In the case of a model composed only of unbranched cylinders originating from the soma (10), except when $\alpha_0 = 0$ (i.e., $\epsilon = 1$),

$$A_{n_{rr}} = \frac{2\psi_{en}(Z_e)\psi_{rn}(X_r)}{\tau_m [g_s(2\epsilon + \theta_n) + \sum_{j \in segs} g_{\infty_j} L_j \sec^2 \alpha_n L_j]}, \quad (37)$$

where

$$\psi_{jn}(X_j) = \frac{\cos \alpha_n (L_j - X_j)}{\cos \alpha_n L_j}. \quad (38)$$

For the n-cylinder, no-soma, no-shunt model, this can be simplified further to give Eq. A11 of Ref. 4. In the case of a single cylinder + soma + shunt model, Eq. 37 can be further simplified: compare with Refs. 29, 30, and 39. For single cylinder + soma models with the shunt omitted, see Eqs. 4.20–4.22 in Ref. 13, and Eqs. 2.11 and 2.12 in Ref. 31.

Special cases requiring Eq. 33 to be modified (see Appendix 4), arise when α_n results from a singularity coincidence in Eq. 22. These can be found using the Laplace transform $\bar{G}$ of the impulse response, given in Appendix 1, and complex residues (following Ref. 10).

An alternative, but less useful derivation of the amplitude terms, using a modified orthogonality relation (32), will be supplied upon request.

Parameter dependence

The important equations determining the solution can be further simplified or rearranged to make clearer their dependence on the "raw" parameters C_m, R_m, R_i, g_{shunt}, d_s, and the l_j and d_j values.

Equation 19 can be written

$$\mu_p = -d_p^{-3/2} \cdot \left\{ \sum_{d \in dtrs_p} d_d^{3/2} \left(\frac{1 - \mu_d \cot(2\alpha l_d \sqrt{R_i/R_m d_d})}{\cot(2\alpha l_d \sqrt{R_i/R_m d_d}) + \mu_d} \right) \right\} \quad (39)$$

since for the jth segment

$$g_{\infty_j} = \frac{\pi}{2} (R_m R_i)^{-1/2} d_j^{3/2}, \quad (40)$$

and the product $R_m R_i$ is uniform over the entire cell.

Equation 22 becomes

$$g_{shunt} = \frac{\alpha^2 a_s}{R_m} + \frac{\pi\alpha}{2\sqrt{R_m R_i}} \sum_{st \in stems} d_{st}^{3/2} \cdot \left(\frac{1 - \mu_{st} \cot(2\alpha l_{st} \sqrt{R_i/R_m d_{st}})}{\cot(2\alpha l_{st} \sqrt{R_i/R_m d_{st}}) + \mu_{st}} \right), \quad (41)$$

where $a_s = \pi d_s^2$ is the soma area.

Except for the case $\alpha_0 = 0$, Eq. 34 becomes

$$E_n = \frac{2}{C_m [a_s + g_{shunt} R_m \alpha_n^{-2} + \sum_{j \in segs} a_j \kappa_{jn}^2 (1 + \mu_{jn}^2)]}, \quad (42)$$

where $a_j = \pi l_j d_j$ is the surface area of segment j. When $\alpha_0 = 0$ (no shunt case),

$$E_0 = \frac{1}{C_m [a_s + \sum_{j \in segs} a_j]}. \quad (43)$$

Notice that, provided $g_{shunt} \geq 0$, and all the other electrical and morphological parameters are positive (as one would expect), E_n is always non-negative.

(i) C_m

The μ_j terms in Eq. 39 and the roots α_n of Eq. 41 are not dependent on C_m. The time constants τ_n are directly proportional to C_m, as can be seen from Eq. 24, using $\tau_m = C_m R_m$. Inspection of Eq. 42 reveals that the E_n and hence all the amplitude terms are inversely proportional to C_m, as would be expected intuitively (since voltage $\propto$ capacitance^{-1}).

(ii) R_m

It can be shown that the roots α_n of the transcendental Eq. 41 are proportional to $R_m^{1/2}$. (If $\alpha = \xi R_m^{1/2}$ then the arguments of the cotangent terms can be written $2\xi l_j \sqrt{R_i/d_j}$, and are therefore independent of R_m. All the μ and κ terms on the right-hand side of Eq. 41 are therefore also independent of R_m, as are the terms $\alpha R_m^{-1/2}$ and $\alpha^2 a_s R_m^{-1}$. Thus the entire equation can be rewritten in terms of the new variable ξ in a form not containing R_m. The roots ξ_n of this equation are independent of R_m, and therefore the original α_n are proportional to $R_m^{1/2}$.) The κ_{jn} and μ_{jn} terms, and the spatial eigenfunctions ψ_{jn} will therefore be independent of R_m.

The time constants can be written as $\tau_n = R_m C_m/(1 + \xi_n^2 R_m)$. For large ξ_n, $\tau_n \approx C_m/\xi_n^2$: the faster time constants are independent of R_m. The slower time constants increase with R_m. The term $g_{shunt} R_m \alpha_n^{-2}$ in the denominator of Eq. 42 is also independent of R_m, and thus so are all the E_n and amplitude terms. The independence from R_m of the initial parts of the responses is also clear from the form of early times solutions for single cylinders (Ref. 2, pp. 41–42) and arbitrary dendritic geometries (12).

(iii) R_i

If g_{shunt} is negligible compared with $\alpha^2 a_s/R_m$, then using the substitution $\alpha = \eta R_i^{-1/2}$, it can be shown that the κ and μ terms and Eq. 41 can also be rewritten in terms independent of R_i, yielding eigenvalues η_n. Thus the larger α_n values (assuming $a_s > 0$, and in the case of $g_{shunt} = 0$, *all* the α_n values) are proportional to $R_i^{-1/2}$, and the corresponding κ_{jn}, μ_{jn}, and ψ_{jn} values are independent of R_i.

The time constants are then given by $\tau_n = \tau_m/(1 + \eta_n^2/R_i)$, and thus the faster ones (i.e., η large) are proportional to R_i. When $g_{shunt} R_m \alpha_n^{-2}$ is negligible compared with the other terms in the denominator of Eq. 42, i.e., when there is no shunt, or for the faster waveform components, the E_n and

amplitude terms are independent of R_i. The slower E_n terms show no simple dependence on R_i when the shunt is nonzero: some may increase, and others may decrease as R_i changes.

Although it has not been proven rigorously, it appears that, whatever the model, all the α_n values decrease with increasing R_i, and hence all the τ_n values increase (except for τ_0 in the zero shunt case, where $\alpha_0 = 0$, whatever R_i).

In a model with a soma but without a shunt, increasing R_i always leads to a decrease in the α_n values, since they are proportional to $R_i^{-1/2}$. It can also be shown for a single cylinder model without a soma, but with a shunt, that $d\alpha/dR_i \leq 0$. To see this, we note that L is proportional to $\sqrt{R_i}$, and thus increasing R_i is equivalent to increasing L. For this model, the transcendental equation (Eq. 41), may be written in the form

$$\alpha \tan(\alpha L) = Lc \tag{44}$$

where $c = R_m g_{shunt}/\pi d l$ is taken as constant. Considering α as a function of L, differentiating Eq. 44, we obtain,

$$\frac{d\alpha}{dL} = \left(\frac{\alpha}{L}\right)\left(\frac{\sin \alpha L \cos \alpha L - \alpha L}{\sin \alpha L \cos \alpha L + \alpha L}\right). \tag{45}$$

Using the inequality $\sin \theta \leq \theta$ for $\theta \geq 0$, Eq. 45 can easily be shown to be negative, and hence α decreases with increasing R_i. Thus $d\alpha/dL$ is negative for single cylinder models both with a soma and a shunt.

In models with a somatic shunt, increases in R_i can have complex effects on the amplitudes: some may increase, while others decrease (although it appears that E_0 always decreases). In models without a somatic shunt, all the amplitude terms are independent of both R_m and R_i: they are determined only by the morphology and C_m.

(iv) g_{shunt}

The right-hand side of Eq. 41 is monotonically increasing with α, so increasing g_{shunt} will shift the roots to larger values of α. The slowest time constants will become smaller. However, since g_{shunt} has progressively less influence upon the eigenvalues as α increases, the fastest time constants and the corresponding κ_{jn}, μ_{jn}, and ψ_{jn} values will be largely independent of the shunt. The corresponding E_n values will also show little dependence on the shunt, since the term $g_{shunt} R_m \alpha_n^{-2}$ in Eq. 42 becomes negligible.

A given α_n must lie somewhere between its value when $g_{shunt} = 0$ and its value when $g_{shunt} = \infty$. However, because the roots of the infinite shunt transcendental equation are the singularities of the zero shunt transcendental equation (see Paper II (36) for discussion), and roots always alternate with singularities, this range must be smaller than the interval between α_n and α_{n+1}, with zero shunt. It therefore follows, that with complex geometries, as soon as the α_n become closely spaced, they cease to increase appreciably with g_{shunt}. In practice, for fully branched geometries based on real neurones (e.g., pyramidal cells), this means that all but the slowest few time constants are almost independent of g_{shunt}.

It can be shown for the n-cylinder model (see Paper II (36), section on Time Constants and R_{ser}) that for small values of $R_{shunt} = 1/g_{shunt}$, $\tau_n \approx \tau_n^{vc} + \beta_n R_{shunt}$, where τ_n^{vc} is the nth time constant from the voltage clamp solution for the same model and β_n is a constant (Paper II, Eq. 58). For the n-cylinder model, the independence from g_{shunt} of the early part of the response can also be seen from the early times solution (Eqs. 4.15 and 4.17 in Ref. 10). The other parameter dependencies for g_{shunt} very large are discussed in Paper II (36) along with imperfect voltage clamp (see "Parameter dependence (imperfect clamp impulse response)"). Numerous simulations have shown that E_0 always decreases with increasing shunt, although subsequent E_n values may either increase or decrease, depending on the model geometry.

In summary, the parameter dependencies of the impulse response waveform components are: fast amplitudes: $\propto C_m^{-1}$, fast time constants: $\propto R_i C_m$, slow amplitudes: $\propto C_m^{-1}$, change with R_i and g_{shunt}, slow time constants: $\propto C_m$, increase with R_i (except τ_0 with zero shunt) and R_m, decrease as g_{shunt} grows.

It should be emphasized that the above amplitude dependencies only apply for the impulse response; convolving with various input functions (see below) introduces further complicating factors into the amplitude expressions which change their relative weightings in a way dependent on how close the corresponding time constant is to the input time constants (e.g., see Eq. 52). In general however, when the input is fast compared with a particular time constant τ_n, the corresponding amplitude term will show roughly the same dependencies as that in the impulse response.

Because both the amplitudes *and* the time constants of the faster components are independent of R_m, changing R_m will not affect the relative weightings of the amplitudes after convolution with a particular input function. Hence, the early parts of all responses, irrespective of the input waveform, will be independent of R_m. Intuitively, this can be explained as follows: axial resistances in typical dendritic trees tend to be much lower than the membrane resistances, so the early phase of charge redistribution is dominated by the membrane capacitance and the cytoplasmic resistance. Only at relatively late times does a significant fraction of the current flow across the membrane resistance (Ref. 2, pp. 41–42). A similar point is illustrated for the voltage clamp case in Fig. 9 *A* of Paper III (37).

When an attempt is made to estimate electrical parameters by matching model impulse transients to real experimental waveforms for a given cell (see Example 1), it can be seen that the fast amplitudes in the data will constrain C_m, and the fast time constants will be important for constraining R_i. The slower amplitudes will be important for constraining g_{shunt} and the slower time constants will finally constrain R_m. If the target data contains insufficient information about either the early or the late components, then some or all of the electrical parameters will be underconstrained and fit nonuniqueness can become a problem (e.g., Refs. 20, 27, 34, 35 and Example 1, below).

RESPONSES TO OTHER INPUTS

The *linearity* of the system can be exploited to obtain the response to any arbitrary *current* input (or initial voltage distribution), by convolution (e.g., Ref. 2, Chapter 13). *Conductance* inputs are not considered here: compartmental models are probably the most convenient tool in such cases.

Current steps (or during current pulse)

The response to a current step of amplitude i_{in} at $t = 0$ is

$$v_r(x_r, z_e, t) = \hat{v}_r(x_r, z_e) - \sum_{n=0}^{\infty} i_{in}\tau_n A_{n_{er}} e^{-t/\tau_n}, \quad (46)$$

where $\hat{v}_r(x_r, z_e)$, given in (Eq. 110) is the steady state voltage: see Appendix 3 for details. Notice that all the amplitude terms are independent of C_m (since $A_n \propto 1/C_m$) and that the fast amplitude terms are proportional to R_i, since $\tau_n \propto R_i C_m$.

The response to a short current pulse can be obtained using Eq. 23 in Ref. 29.

"Alpha" function currents

Some synaptic currents are thought to be well approximated by functions of the form

$$i(t) = Qa^2 te^{-at}, \quad (47)$$

(e.g., Refs. 40 and 41), where a is the inverse of the time-to-peak and Q is the total charge injected. The waveform obtained by convolving an "alpha" function with the impulse response is

$$v_r(x_r, z_e, t) = \sum_{n=0}^{\infty} \frac{Qa^2 A_{n_{er}}}{(1/\tau_n - a)^2} \cdot [e^{-t/\tau_n} + e^{-at}\{t(1/\tau_n - a) - 1\}] \quad (48)$$

(compare with Ref. 42, p. 208, Eq. 5.62). Special cases arise when $a = \tau_n^{-1}$. These can be avoided in practice by changing a by a small amount (<1 in 10^{-8}). All the $t(1/\tau_n - a)e^{-at}$ terms can be lumped together (see Appendix 2).

Multiexponential currents

Recent experimental evidence (e.g., Ref. 43) suggests a good approximation to synaptic currents may be a waveform composed of one or more exponentially decaying components with different time constants τ_{sy_n}.

In response to a current decaying with a single time constant τ_{sy}

$$i(t) = \frac{Q}{\tau_{sy}} e^{-t/\tau_{sy}}, \quad (49)$$

the voltage response is

$$v_r(x_r, z_e, t) = \sum_{n=0}^{\infty} \frac{QA_{n_{er}}}{(1 - \tau_{sy}/\tau_n)} [e^{-t/\tau_n} - e^{-t/\tau_{sy}}]. \quad (50)$$

A commonly used variant is the dual exponential current:

$$i(t) = \frac{Q}{\tau_{sy_1} - \tau_{sy_2}} (e^{-t/\tau_{sy_1}} - e^{-t/\tau_{sy_2}}), \quad (51)$$

(compare with Ref. 44, p. 327). The response is

$$v_r(x_r, z_e, t) = \sum_{n=0}^{\infty} QA_{n_{er}} \left[\frac{\tau_n^2}{(\tau_n - \tau_{sy_1})(\tau_n - \tau_{sy_2})} e^{-t/\tau_n} + \frac{\tau_n \tau_{sy_1}}{(\tau_{sy_1} - \tau_{sy_2})(\tau_{sy_1} - \tau_n)} e^{-t/\tau_{sy_1}} + \frac{\tau_n \tau_{sy_2}}{(\tau_{sy_2} - \tau_{sy_1})(\tau_{sy_2} - \tau_n)} e^{-t/\tau_{sy_2}} \right]. \quad (52)$$

Again, special cases arise when one of the synaptic time constants τ_{sy_n} is the same as one of the cell time constants τ_n. See Appendix 2 for a discussion of how to lump together all terms of the form $e^{-t/\tau_{sy_n}}$, to improve accuracy and speed.

IMPLEMENTATION

The taming of the transcendental equation

A root-finding algorithm is necessary for solving the recursive transcendental equation (Eq. 22). If time constants smaller than τ_{min} are not required, (Eq. 24) implies that the search for eigenvalues can be limited to $\alpha \leq (\tau_m/\tau_{min} - 1)^{1/2}$.

The function

$$g_s \left[\frac{\epsilon(1 + \alpha^2) - 1}{\alpha} \right] + \sum_{st \in stems} g_{x_{st}} \left(\frac{1 - \mu_{st} \cot \alpha L_{st}}{\cot \alpha L_{st} + \mu_{st}} \right) \quad (53)$$

is straightforward for simple geometries like a soma-single cylinder (e.g., Ref. 29, Fig. 2). Models based on real neuronal morphologies (e.g., the hippocampal CA1 pyramidal cell in Example 1 and Fig. 2) can produce very complicated transcendental functions which resemble the superposition of several tangent curves of differing periodicities (e.g., see Fig. 5). Between neighboring singularities, the function Eq. 53 increases monotonically. At some point in this interval, as it crosses the α axis moving from negative to positive values, a zero occurs. The value of the function can vary dramatically and unpredictably with extreme irregularity in the spacing of the singularities along the α axis. This is true even of the simple case of two coupled segments with no soma or shunt. The variable intervals between singularities can pose a serious challenge to any root-finder which simply marches along the α axis looking for positive-going zero-crossings, however sophisticated its "homing in" strategy. It can never be guaranteed to find all the eigenvalues in the range of interest, because there will always be the possibility of inter-singularity intervals much shorter than its minimum search increment, and the corresponding zeros will be missed.

Careful examination of Eq. 22 suggests a *recursive root-finding algorithm* which will not miss any zeros of (Eq. 53): first find the singularities of the function, and then search the interval between neighboring pairs of singularities for the

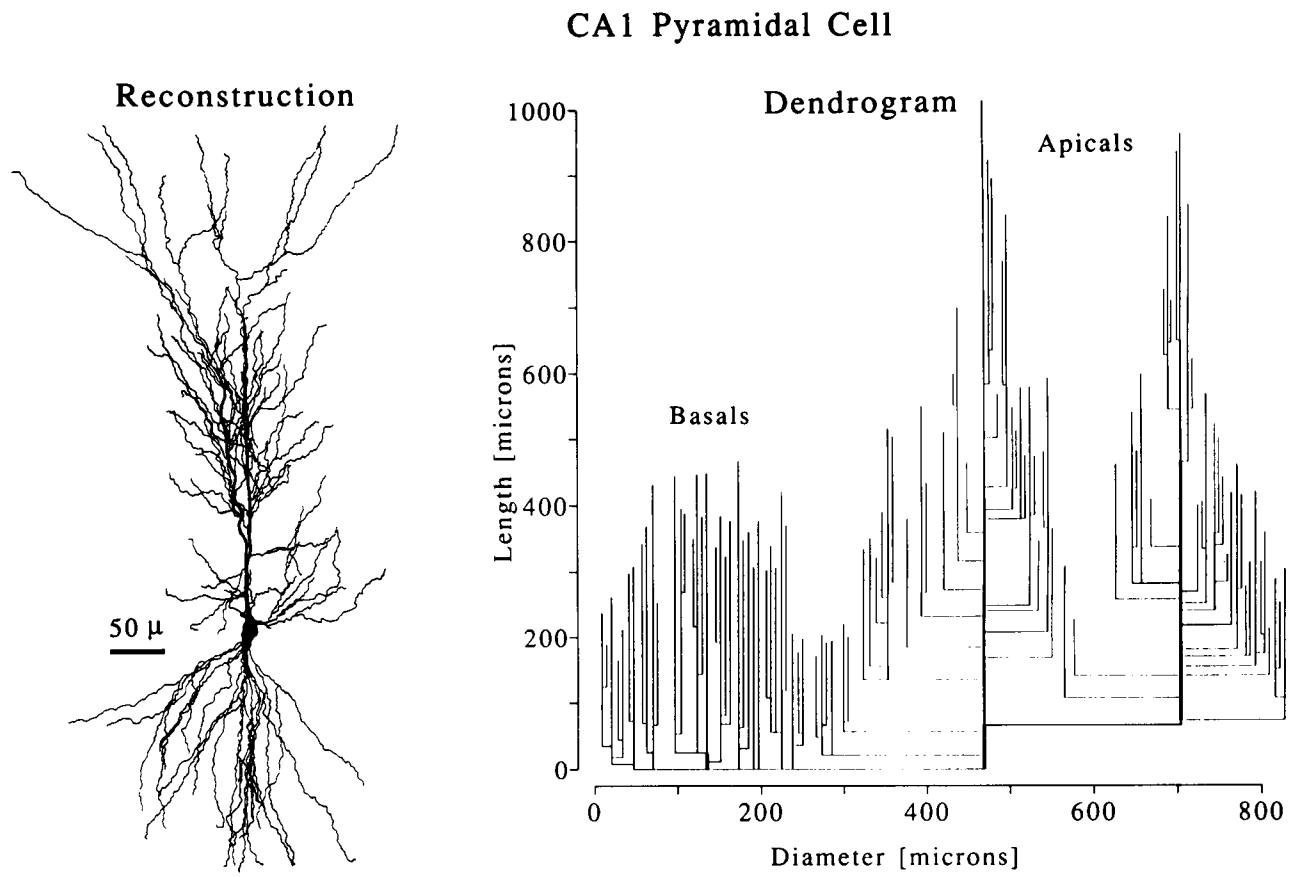

FIGURE 2 The rat hippocampal CA1 pyramidal neurone (used in Example 1 and Fig. 1). On the left is a *camera lucida* reconstruction of the cell, which was filled with biocytin and reacted with avidin-horseradish peroxidase. On the right is a dendrogram of the same cell: vertical lines indicate the relative lengths and diameters of segments, following a "spine collapse" procedure which increases the length of each segment by a factor of $F^{2/3}$ and the diameter by a factor of $F^{1/3}$, where F is the ratio, for that segment, of the surface area with spines to the surface area without spines.

zeros, by means of "binary chopping." (If the value of the function at the mid-point of the interval is negative, search the right-hand half-interval. If the value is positive, search the left-hand half-interval, and so on, until the absolute value of the function is smaller than some criterion, at which point a root of Eq. 22 has been "found."

A dummy singularity is assumed at a small negative value of α to limit the search on the left. A singularity in Eq. 53 occurs whenever there is a singularity contributed by one of the subtrees (with parent segment d) originating from the soma: a singularity in one is a singularity in all. The singularities from individual subtrees will be scattered in some fashion along the α axis. If there is more than one subtree, the various contributions must be *merged* into a single sorted list before the intervals are binary-chopped.

A subtree singularity occurs whenever the corresponding denominator term in Eq. 53, the function

$$\cot \alpha L_d + \mu_d \tag{54}$$

is zero (for special cases, see Appendix 4).

Therefore, in order to find the subtree singularities of Eq. 53, it is necessary to find the zeros of the negative value of function Eq. 54 which, like Eq. 53, is monotonic increasing between singularities. Those singularities originating from the cotangent term occur whenever $\alpha_n = N\pi/L_d$, for integers $N \geq 0$. The others are the singularities of μ_d. Any daughter segment j of d which is a termination, will contribute to μ_d the term $-g_{\infty_j} \tan \alpha L_j$, which has singularities at $(2N + 1)\pi/2L_j$. Nonterminal daughters will contribute terms with singularities whenever their denominators, also of the form of Eq. 54, are zero. These can be found by recursing down the tree until eventually the tips are reached. Once all the singularities of a subtree have been found and ordered, the intervals between them can be binary chopped to find the zeros of Eq. 54, and hence the singularities for the next level up the tree toward the soma.

Every time a generation in a subtree is ascended (going back toward the soma), the last singularity obtained from the previous level's zeros is at a progressively smaller value of α. In order to find all the relevant zeros of Eq. 53, at the level of the soma (i.e., the eigenvalues), it is necessary to include one further zero along the α axis, of the appropriate function (Eq. 54), per generation descended from soma to tips. Without this precaution, time constants in the range of interest may be missed.

Programs

An ANSI-C program has been written to find the α_n values, by means of the recursive algorithm described above, and

hence to calculate the τ_n and A_n values and waveforms for various input functions, and stimulation and recording positions. Another program fits these model waveforms *directly* (14, 20, 45) to experimental responses by adjusting parameters under the control of a simplex algorithm (Refs. 46, 47 (p. 305)). Programs and further details of implementation will be supplied upon request.

APPLICATIONS

Example 1: Hippocampal CA1 pyramidal cell

Full model

Morphological data were obtained from an adult rat hippocampal CA1 pyramidal neurone filled with the marker biocytin during an in vitro slice experiment and reacted with avidin-horseradish peroxidase after fixation (Ref. 34, Chapter 5). The cell was drawn and reconstructed with a light microscope and *camera lucida* under high power (×100 oil immersion objective, Fig. 2, left). Estimates were made, for all segments, of their diameters and their lengths within the plane (34). Each segment's end-to-end displacement perpendicular to the plane of section was also measured using the fine focus. To obtain an estimate of the actual length in three dimensions, Pythagoras' theorem was applied. The length was then multiplied by an additional "wiggle" factor (in this case, 1.2), to account for snaking up and down perpendicular to the plane of section. Dendritic spines were counted on a subsample of segments of different classes and diameters, lying fairly flat in the plane. Graphs of spine density versus diameter were prepared (e.g., basal dendrites with a diameter of 0.6 μm had about 3.2 spines μm^{-1}). The cell had roughly 36,000 spines in all. Single spine areas were assumed to be 0.83 μm^2, taken from a serial electron microscopy study (Ref. 48, Table 2).

The data was entered into a computer file, and spines were collapsed into their dendritic shafts of origin (Refs. 20, 49, 34 (Appendix B), see also Fig. 2 legend). This "full" morphological specification is portrayed in the dendrogram in Fig. 2 (right) and summarized in the middle of Table 2.

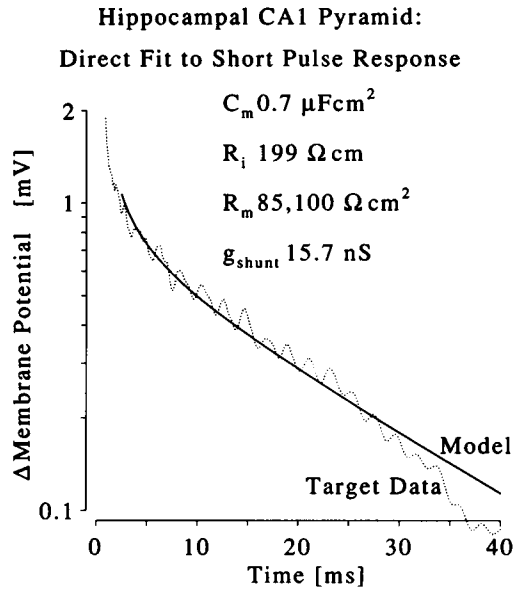

FIGURE 3 Illustration of direct fitting, using the hippocampal CA1 pyramidal cell. Recording from the soma. Fit interval 2.5–40 ms. The real cell's experimentally recorded response to a +0.5 nA somatic short current pulse (duration 0.5 ms) is the noisy dotted line (average of 200 sweeps, scaled by a factor of 2 to normalize it to 1 nA, digitally smoothed with a $\sigma = 0.05t$ variable Gaussian filter: see Ref. 34, Appendix A). Note logarithmic voltage axis. When C_m was fixed to 0.7 μFcm^{-2} and R_i to 199 Ωcm, the optimal values of R_m and g_{shunt} were 85,100 Ωcm^2 and 15.7 nS, respectively. A model with these electrical parameters and the morphology specified in Fig. 2, given a somatic input current of 1 nA, duration 0.5 ms, yielded the solid waveform. *Fit nonuniqueness*: acceptable fits could be found with C_m fixed at any value between 0.65 and 0.825 μFcm^{-2}: these all had R_i values close to 200 Ωcm, but R_m varied between 133,000 and 46,000 Ωcm^2 and g_{shunt} varied between 17.9 and 11.1 nS, respectively. See Ref. 34 (Chapter 5) for more details.

TABLE 2 Selected details of CA1 pyramidal cell model

C_m	0.7	μFcm^{-2}
R_m	100,000	Ωcm^2
R_i	200	Ωcm
g_{shunt}	15.0	nS
d_s	17.0	μm
Stem segments	9	
Segments	190	
Branch points	87	
Terminations	103	
d_{basal}*	0.79	μm
$d_{oblique}$*	0.74	μm
d_{tuft}*	0.57	μm
Maximum tree depth	22	
Surface area	64,420	μm^2
τ_m	70	ms
g_{sm}	0.0908	nS
ϵ	0.0060	
Stems' total g_∞	8.08	nS
Maximum L_{eff}‡	0.39	

* Average diameters of terminal segments of subscript $_{class}$, after spine incorporation.
‡ See Eq. 114.

Electrical parameters

The four electrical parameters selected for the model are listed at the top of Table 2. They are loosely based on the results of directly fitting the short pulse response of the full model to that of the real cell (see Fig. 3 and Ref. 34 (Chapter 5), for details). The value of C_m of 0.7 μFcm^{-2} was a compromise based upon typical optimal values found from direct fits of short pulse responses in both cortical and hippocampal pyramidal neurones (34), and direct measurements on lipid bilayers (50, 51), erythrocytes (52, 53) and squid giant axons (nonfrequency-dependent component) (54, 55, 56). A sharp electrode was used for the recording, which may explain the large shunt (approximately 15 nS). This in turn led to a high R_m of the order of 100,000 Ωcm^2 being required to match the final decay of the experimental waveform. The R_i of 200 Ωcm, high compared with "traditional" values closer to 70 Ωcm, was required to fit the early components of the cell's response (see Ref. 34 for discussion).

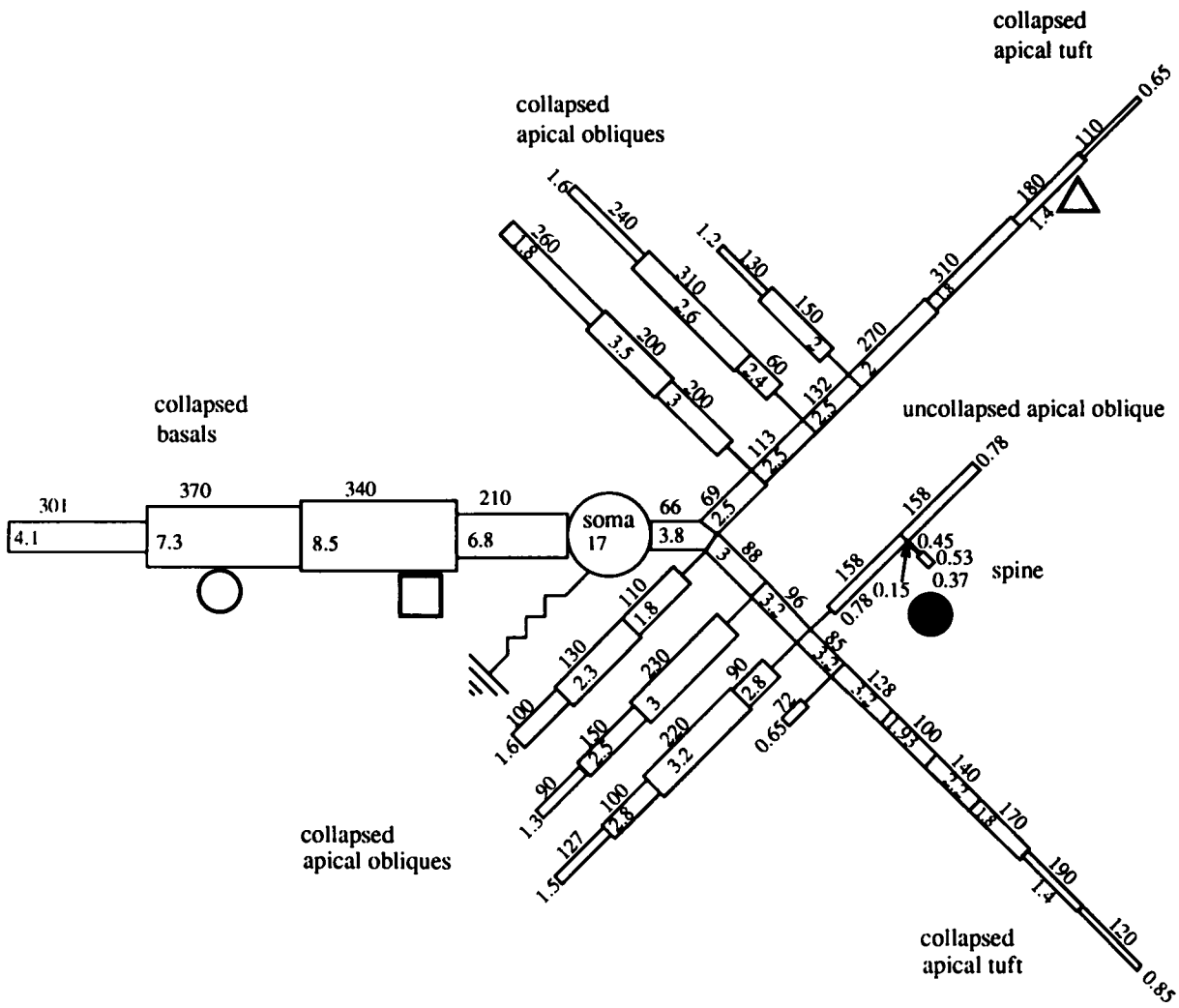

FIGURE 4 "Cartoon" representation of the CA1 pyramid in Fig. 2. Above each segment is its length, and within it, at one end or just below, is its diameter. The model has a somatic shunt, and receives an input onto a dendritic spine (*center right*). The spine dimensions are: neck diameter, 0.15 μm; neck length, 0.45 μm; head diameter, 0.37 μm; head length, 0.53 μm. The other symbols mark input and recording sites used in Paper III: □, proximal basal (segment 2, 65 μm); ○, mid basal (segment 3, 214 μm); ●, apical oblique (spine head: segment 26, 0 μm), △ apical tuft (segment 19, 81 μm).

Equivalent dendrite collapses

Following Ref. 20, a simplified representation of the full morphology was prepared, using equivalent dendrite collapses. A group of subtrees, of roughly the same relative electrotonic length, are aligned at their origins. Each segment j then has its length adjusted by the transformation $l'_j = l_j/\sqrt{d_j}$. All lengths are now in terms of *relative electrotonic distance* x' from the origin. The subtrees must now be combined or collapsed together. Moving away from the origin, at regular intervals (e.g., every "$\mu m^{1/2}$"), the diameter $D(x')$ of the electrically equivalent cylinder is calculated using the 3/2 Rule (e.g., Ref. 13): $D(x') = (\Sigma\, d_j(x')^{3/2})^{2/3}$, where the summation is over all segments at that relative electrotonic distance x' from the origin. The resulting equivalent dendrite is divided into segments c of constant diameter D_c and relative electrotonic length l'_c. Finally, to ensure total surface area is conserved, the transformation $l''_c = l'_c\sqrt{D_c}$ is applied to each of these segments, to give its *physical* length l''_c. For further discussion of $l/\sqrt{d}$-based transformations see Refs. 27 and 57.

"Cartoon" representation

A simplified "cartoon" representation of the cell, following Stratford et al. (20), is summarized in Fig. 4. All the basal dendrites were combined into a single equivalent dendrite. Likewise, groups of apical oblique dendrites originating within 100 μm of one another were collapsed together, and the equivalent dendrite was reattached to the apical trunk at a point midway between the origins of its component obliques (weighted toward the bigger ones). Each apical tuft was also collapsed. The resulting structures were represented

TABLE 3 Waveform components from CA1 pyramidal cell models

	Full Model					Cartoon representation			
n	α_n	τ_n (ms)	E_n* (mV)	amp_{146s}‡	n	α_n	τ_n (ms)	E_n* (mV)	amp_{26s}‡
0	1.34	25.11	1.266	0.193	0	1.36	24.66	1.346	0.203
1	2.36	10.64	0.206	0.067	1	2.57	9.21	0.215	0.083
2	2.86	7.61	0.218	−0.076					
3	3.19	6.28	0.042	−0.001	2	3.18	6.30	0.472	−0.151
4	3.37	5.67	0.005	0.001					
5	3.40	5.56	0.000	0.000					
6	3.48	5.34	0.017	0.012					
7	3.55	5.14	0.010	0.015					
8	3.61	4.99	0.006	0.029					
9	3.65	4.88	0.000	−0.001	3	3.83	4.47	0.061	−0.010
31	5.18	2.51	0.237	−0.035	7	6.19	1.78	0.044	−0.013
42	6.03	1.87	0.134	0.105	8	6.39	1.67	0.181	0.012
53	7.42	1.25	0.110	−0.003	9	6.90	1.44	0.132	−0.011
54	7.54	1.21	0.115	−0.003					
55	7.64	1.18	0.128	−0.000					
59	7.84	1.12	0.190	−0.002	10	7.81	1.13	0.003	0.003
65	8.68	0.92	0.154	0.012	11	8.61	0.93	0.075	0.000
66	8.74	0.91	0.212	0.002	12	9.11	0.83	3.21	0.006
448	59.16	0.02	0.118	0.000	78	59.04	0.02	0.563	0.000
sy_1		0.10		0.095	sy_1		0.10		0.004
sy_2		2.00		−0.005	sy_2		2.00		0.349

* $\times 10^{-12}$. Equivalent to amplitude of somatic response to 1 pC somatic point charge.

‡ Amplitudes [mV] of somatic response to double exponential current: total charge 0.1 pC, τ_{sy_1} 0.1 ms, τ_{sy_2} 2 ms, injected 158 μm into segment 146 of the full model (Fig. 2) or into the spine head (segment 26) in the cartoon representation (Fig. 4).

by between one and five segments of fixed diameters (equal to the average diameter over the corresponding length of the equivalent dendrite). Care was taken to ensure that the overall surface area was very close (within 0.01%) to that of the full model (64,420 μm^2). One apical oblique dendrite was left uncollapsed. All the spines in this dendrite were collapsed into the shaft except one, which was to be the site of a synaptic input. This spine (with the median dimensions in Table 2 of Ref. 48 was attached half way along the dendrite. In Fig. 4 it can be seen that the cartoon represents the essential structure of the full model (basal tree with some initial flare and final taper, bifurcating apical trunk, a large number of apical obliques, tapering apical tufts). Above each segment is written its length [μm], and within, at one end or just below it, its diameter. For clarity, segment numbers are omitted; with a left-first, depth-first scheme the basal stem would be segment 1, and the spine head would be segment 26.

Comparison of full model and cartoon

Both models were given the same electrical parameters (Table 2, top). Identical inputs were injected into corresponding points on their dendritic trees: half way along segment 146 in the case of the full model, and in the spine head of the cartoon. This apical oblique site would probably have received a Shaeffer collateral input in the original cell. The input used was a double exponential current: total charge 0.1 pC, τ_{sy_1} 0.1 ms, τ_{sy_2} 2 ms. These figures are consistent with recent glutamate pulse experiments on AMPA receptors in excised patches from hippocampal slices (43), and give a time-to-peak current of about 0.3 ms. The total charge was deliberately chosen so that the peak response at the soma was about 120 μV (see Fig. 6), comparable to the mean quantal amplitudes in Ref. 58. Further synaptic potentials from these models are shown in Fig. 8 *A* of Paper III (37).

Table 3 lists for both models some of the eigenvalues α_n, their associated time constants τ_n [*ms*], their *position-independent* amplitude components E_n ($\times 10^{-12}$) [mV] (Eq. 34) and the amplitudes in response to the synaptic inputs described above. In the lower half of the table, only components with relatively large E_n values are listed, (up to n = 66 for the full model, and n = 12 for the cartoon). Components contributing to similar portions of the waveforms are crudely aligned to facilitate comparison.

A plot of part of the transcendental function (Eq. 53) for a full model of the same cell with slightly different parameters is shown in Fig. 5. Note the extreme irregularity in the spacing of the singularities and zero-crossings.

It can be seen that for the 190-segment full model: (i) many of the time constants are very close to one another, (ii) the majority of them have relatively small E_n values, (iii) nearly 450 components are required to obtain τ_n values below 0.02 ms. A component with this time constant might exert an effect out to about 0.1 ms, depending on the size of its corresponding E_n.

In the case of the 44-segment cartoon representation: (i) the time constants are more widely spaced, (ii) the E_n values are usually larger than those of the full model: roughly speaking, several full model terms become "lumped" together to give each cartoon term (for $n > 2$), (iii) only 78 components are required to achieve $\tau_n < 0.02$ ms.

Although the lumped terms (sy_1 and sy_2) and all but the first two components listed in Table 3 are very different for

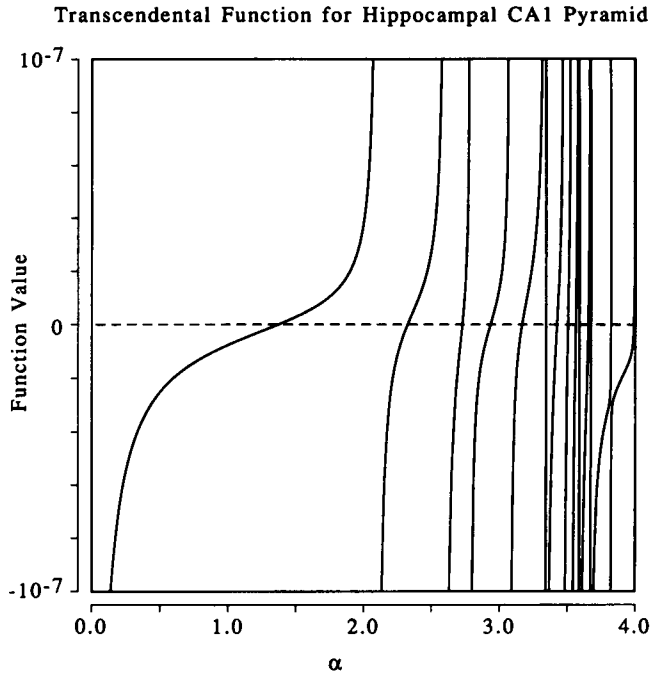

FIGURE 5 Plot of part of the transcendental function (Eq. 53) for a model of the CA1 pyramidal cell in Fig. 2. Notice the extreme irregularity in the spacing of the zero-crossings (roots) and singularities.

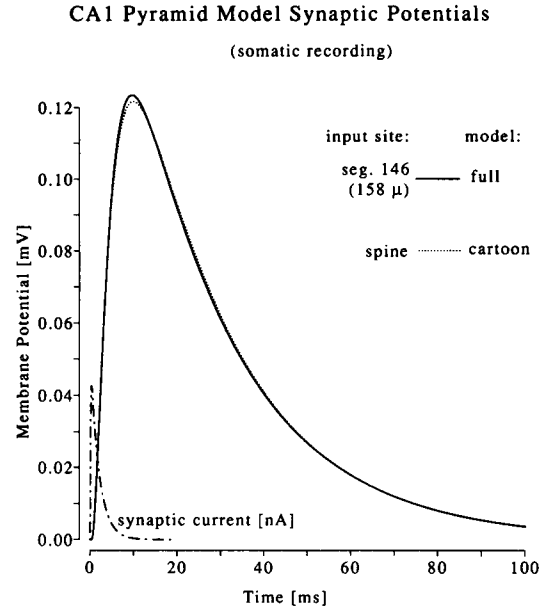

FIGURE 6 Somatic voltage responses of the full and cartoon CA1 models compared. The inputs are to corresponding points in the two models: a typical apical oblique segment, probably receiving synapses from Schaeffer collaterals (● in Fig. 4 above and also Fig. 7 of Paper III: segment 146, 158 μm in the full model). The current is a double exponential function, with total charge 0.1 pC, τ_{sy_1} 0.1 ms and τ_{sy_2} 2 ms.

the two models, the corresponding waveforms in (Fig. 6) are remarkably similar. The cartoon also reproduces the full model response reasonably faithfully when other input or recording sites are tested, under both voltage recording and voltage clamp (see Paper III (37)), providing the two locations are not both in the same collapsed segment.

Responses were recorded both from the soma and dendritic segments of the cartoon. Virtually no difference was observed between the transients generated by spine head inputs and those resulting from the same inputs into the parent shaft at the spine base (not shown). Indeed, removing the spine altogether had a negligible effect on the component time constants and amplitudes in Table 3.

Despite the slow convergence of the exponential series (Eq. 1) for the full model, the waveform generation program required only about 114 C.P.U.s (central processor unit seconds) on a SUN 4/SPARC-2 workstation to find about 450 eigenvalues. (Only 5 C.P.U.s were required to find 80 roots using the cartoon, which is a considerable increase in speed.) Once the roots had been found (or read in), about 6 C.P.U.s were required to calculate the κ_{jn} values, and 8 C.P.U.s were required per 100-ms waveform. A compartmental model of the same cell with the same parameters, run using an existing package (14), written in Fortran-77 and compiled with optimization, required just over 400 C.P.U.s on the same processor to generate 100 ms of waveform (although it could generate responses from up to 10 recording positions at once). This model had 15 compartments per space constant and consisted of a total of 553 compartments. The program used an *explicit* integration method; the time step required (for stability) was 0.5 μs. Implicit methods (e.g., Ref. 15) would be able to use a longer time step and, as a result, might be faster, although systematic benchmarking has not been performed.

In other comparisons, transients were generated by the compartmental model using 99 compartments per space constant in the input and recording segments, to achieve the maximum allowed accuracy in the positioning of the stimulation and recording positions. The corresponding analytic solution waveforms were indistinguishable, except for "artifacts" lasting out to about 0.1 ms. These were due to the omitted components (those with time constants faster than τ_{448}).

The accuracy and efficiency afforded by cartoon representations may be particularly useful in active compartmental models, given the potentially large number of state variables per compartment.

Example 2: Two cylinder + soma + shunt model

Visual cortical pyramidal cell simplified representation

The second example is much simpler, but illustrates several important features of the branching-geometry analytic solution. The model is based *very loosely* upon a simplified representation of a typical adult rat layer III visual cortical pyramidal neurone, shown in Fig. 7 (34); see Ref. 59 for other examples. The dendrites of this cell fall into two groups with very different physical lengths, as can be seen from the dendrogram in Fig. 7 (right): (i) the basals and apical obliques and (ii) the apical trunk plus tuft. This dichotomy is even more pronounced when relative *electrotonic* lengths are compared (Ref. 34, Chapter 3).

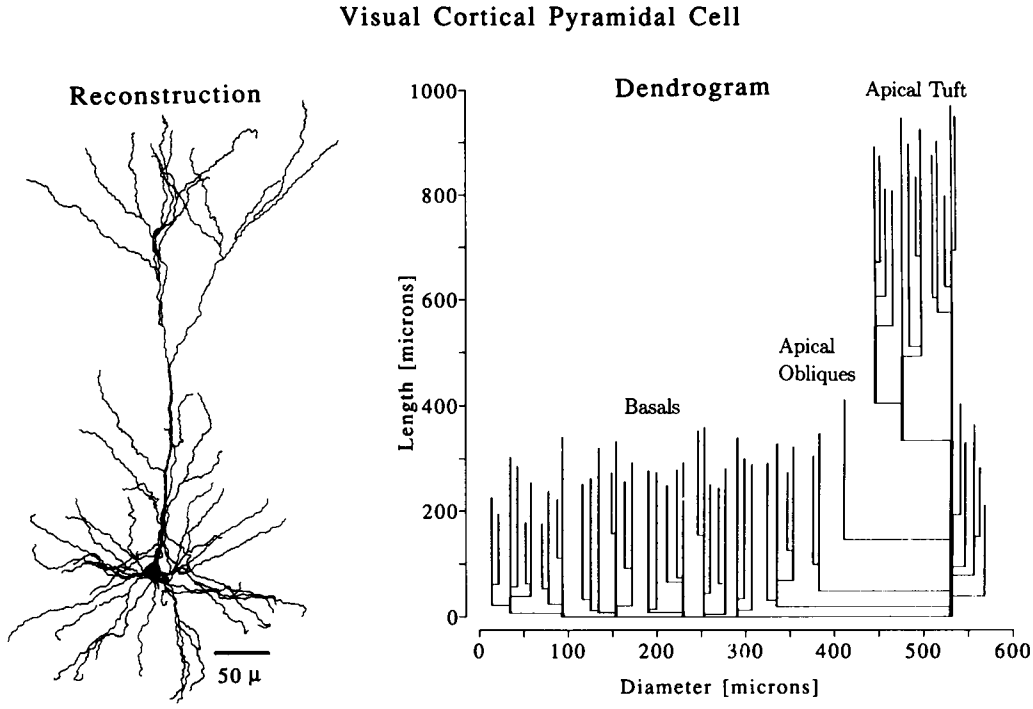

FIGURE 7 Representations of a layer III rat visual cortical pyramidal neurone, upon which the double cylinder model in Example 2 (Fig. 8) is loosely based. Notice that the basal dendrites and apical oblique dendrites seem to form one group with very similar physical lengths (after spine collapse), while the apical tuft segments form a second group terminating much further away from the soma.

Single spine areas were assumed to vary with dendritic diameter d in the following manner: $d \leq 1.5$ μm: 1.7 μm^2, 1.5 μm $< d <$ 2 μm: 1.5 μm^2, d $\geq$ 2 μm: 1.4 μm^2 (57, 60, 61). Spine collapses were carried out on all the dendrites. The apical oblique dendrites were then stripped from the apical trunk and attached directly to the soma. One equivalent dendrite collapse was performed on the basal/oblique tree and another on the remaining apical tree. Finally, this simplified representation was further idealized, by "squaring off" the resulting near-cylinders to obtain the double cylinder representation in Fig. 8 and Table 4. In Fig. 8, the short, fat dendrite on the left ("basal") corresponds to the collapsed basal and apical oblique dendrites. The long, thin dendrite on the right ("apical") corresponds to the apical trunk and tuft. This model is *not* an adequate representation of the neurone: it has a different surface area, and its charge equalization characteristics are less complex than those of the full geometry (it produces far fewer exponential components for a given cut-off τ). It does, however, capture one very important feature: the two classes of dendrites with very different relative electrotonic lengths.

Responses and "slow bends"

The "raw" electrical and morphological parameters of the model are listed at the top of Table 4, and the "core" model parameters are listed below them (see Discussion for further explanation). The "traditional" value for C_m, 1 μFcm^{-2}, is used. R_i and R_m are close to the optimal values found for this cell by directly matching model to experimental short pulse responses (Ref. 34, Chapter 4). A large shunt of 100 nS is used, to accentuate the slow bends, i.e., slow increases in apparent τ_0 as the fit interval is made progressively later (see below). Table 5 contains a partial list of the output of the waveform generation program when given this model as input. The time constants apply over the entire cell, irrespective of input and recording sites. (Note that τ_m = 50 ms.) The unit impulse (1 pC) response amplitudes $A_{n_{er}}$ [mV] vary with input and recording site (e and r, respectively) and are unaltered if these sites are interchanged (a symmetry implied by the $\leftrightarrow$ notation): four examples are given. Again, the waveforms, plotted in Fig. 8, are indistinguishable from the equivalent compartmental model output, except for the initial artifact. In the cases shown, enough exponential components were included to effectively remove the artifact.

The waveforms are re-plotted using semi-logarithmic axes in Fig. 8 *B*. After about 12 ms ($\approx 5\tau_2$), the different relative sizes of A_0 and A_1 in the various solutions are largely responsible for the markedly different degrees of curvature or bend that can be seen.

In Table 6 are the results of estimating for each waveform the apparent decay time constant τ_{eff} over two intervals (20–30 and 40–50 ms). Linear regression is used to fit a straight line through the ln(v) against t values; once the slope and intercept are known, τ_{eff} is given by

$$\tau_{eff} = -1/\text{slope}. \tag{55}$$

In the last column of Table 6, the ratio between the two τ_{eff} values is given. The positive ratios and τ_{eff} values greater

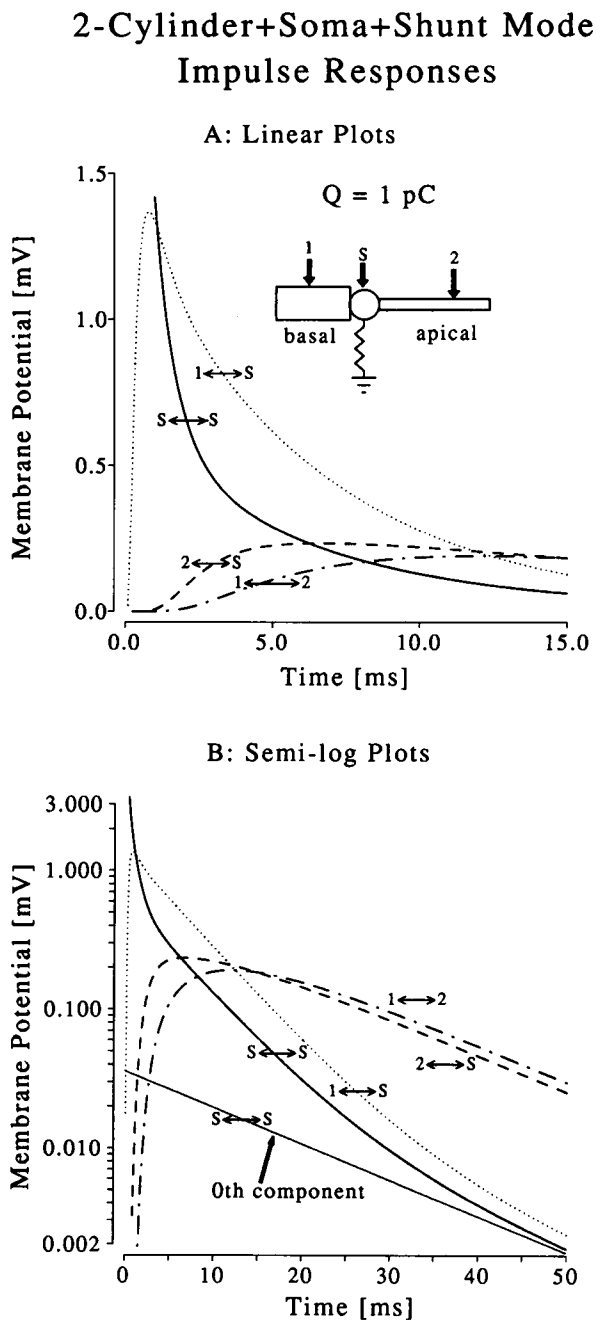

FIGURE 8 Responses to 1 pC instantaneous point charges (impulses) of a model based on a simplified representation (see A, inset) of the layer III pyramidal cell in Fig. 7. The right hand or "apical" (trunk + tuft) equivalent cylinder is much longer and thinner than the left hand or "basal" (basals + obliques) cylinder. The injection and recording sites are marked by arrows. The basal dendritic input site is located halfway along the basal equivalent cylinder (x_1/l_1 = 500 μm/1000 μm), and the apical input is two thirds of the way along that equivalent cylinder (x_2/l_2 = 1000 μm/1500 μm). Each waveform is labeled with the particular input site (e) and recording site (r) used to generate it ($e \leftrightarrow r$) Notice that the waveforms are not affected by exchanging these two positions, as the $\leftrightarrow$ notation implies. For example, the "synaptic" potential $1 \leftrightarrow S$ recorded at the soma by stimulating site 1 is identical to the transient recorded at site 1 in response to a somatic impulse. See Table 4 for details of the model parameters and Table 5 for information about the component time constants and amplitudes of these transients. (A) Linear voltage axis. (B) Logarithmic voltage axis to illustrate slow "bends" in the "apparent time constant," τ_{eff}. The slowest (0th) component, $A_{0_{ss}}e^{-t/\tau_0}$, of the soma-to-soma waveform ($S \leftrightarrow S$) is also shown. Over a

TABLE 4 Details of two-cylinder + soma + shunt model

"Raw" parameters		
C_m	1.0	μFcm^{-2}
R_m	50,000	Ωcm^2
R_i	250	Ωcm
g_{shunt}	100	nS
d_s	15.0	μm
l_1	1,000	μm
d_1	10.0	μm
l_2	1,500	μm
d_2	4.0	μm
"Core" parameters		
τ_m	50.0	ms
g_s	100.14	nS
ϵ	0.0014	
L_1	0.447	
g_{∞_1}	14.05	nS
L_2	1.061	
g_{∞_2}	3.56	nS
Dendritic recording sites		
x_1*	500	μm
X_1	0.224	
x_2*	1,000	μm
X_2	0.707	

* Arrowed sites in Fig. 8.

than τ_0 for cases $2 \leftrightarrow S$ and $1 \leftrightarrow 2$ arise because during the intervals chosen, particularly the first, the contribution of a large negative A_1 is still significant, and the semilog-plots of the waveforms are convex upwards. The other two cases, however, have small A_0 values and large positive A_1 values. After about 12 ms, the voltage decay is dominated by τ_1, until *very* late times (after 45 ms), when τ_{eff} tends slowly towards τ_0. The contribution of A_1 relative to A_0 diminishes with time, and the semi-log waveform appears to undergo a slow bend as its gradient swings away from $-1/\tau_1$ and toward $-1/\tau_0$.

The pitfalls of applying crude methods for estimating the final decay time constant are obvious in the example given, both because the data are noise-free, and because the underlying A_n and τ_n values are already known. In the experimental situation, however, where noise can obscure waveforms at late times, and where distortions may be introduced by active conductances, particularly "sag" (e.g., Refs. 33, 34, 62, 63), the following errors may occur while trying to estimate τ_0: (i) regression over an interval where a large amplitude early component with the opposite sign to A_0 is still significant and the semi-log waveform ($\times -1$, if A_0 is negative) is convex upwards, (ii) regression during a slow bend, (iii) regression during an apparently linear phase of decay (on the semi-log plot), where bend and sag cancel out, (iv) regression over an interval where the apparent time constant has been prolonged by any active conductance with effects opposite to sag.

All of these errors can lead to apparent τ_0 values that may bear little relation to the "real" value: they can be either

particular interval, τ_{eff} depends on the input and recording position: where at least one of these is a distal apical site (2), τ_{eff} after 12 ms is much longer than for cases where only the basal dendrite (1) and/or soma (S) are involved (see Table 6). Only at very late times do the apparent time constants of the different waveforms all converge on the actual τ_0 of 16.5 ms.

TABLE 5 First ten components of waveforms* in Fig. 8

n	α_n	τ_n ms	$A_{n_{1_s}}$ mV	$A_{n_{1_1}}$ mV	$A_{n_{2_2}}$ mV	$A_{n_{12}}$ mV
0	1.42	16.50	0.036	0.042	0.524	0.619
1	2.71	5.99	0.581	1.361	−0.347	−0.811
2	4.38	2.47	0.040	−0.059	−0.013	0.020
3	7.14	0.96	0.700	0.018	−2.052	−0.053
4	8.57	0.67	2.449	1.081	2.574	1.136
5	10.38	0.46	0.003	0.031	−0.149	−1.478
6	13.07	0.29	0.687	−0.741	−0.232	0.250
7	14.78	0.23	3.510	−3.660	−1.729	1.801
8	16.44	0.18	0.229	−0.410	1.274	−2.283
9	19.09	0.14	0.290	0.198	1.474	1.006

* Generated by injecting 1 pC point charges into model in Table 4.

greater or smaller. "Peeling" (3), to obtain further time constants, is very sensitive to errors in the components stripped away: even a relatively small error in τ_0 can lead to serious errors in τ_1. Exponential fitting or transform-based methods *may* lead to smaller errors in τ_1, depending on how the data is weighted (e.g., Ref. 4).

It is worth noting that different fractional errors in τ_0 and τ_1 will cause errors in estimates of a single L value based on the τ_0/τ_1 ratio (Eq. 3 in Ref. 3). In any case, L values obtained employing this commonly used formula may be misleading for a number of other reasons, for example:

(i) The cell may have a large soma relative to its dendritic tree, in which case Eq. 23 of Ref. 3 combined with Eq. 6 of Ref. 64 can be used to obtain a better estimate of L, (providing there is no somatic shunt). Alternatively, fitting algorithms based on the solutions in Refs. 3 and 13 can be used.

(ii) There may be a somatic shunt. If so (which seems a reasonable possibility for most sharp electrode recordings), methods based on the solutions in Refs. 29 and 30 should be used, bearing in mind problems of fit nonuniqueness (e.g., 20, 26, 34, 35, 65, 82).

(iii) The cell may have dendrites of very different electrotonic lengths (4, 66, 67). This is the case for many pyramidal neurones (e.g., 20, 34, 57, 68) and motoneurones (e.g., 35, 45, 69, 70).

DISCUSSION

The solution

Generalizing the results from previous studies (3, 10, 13, 29, 30, 31, 39), the following solution has been derived for the impulse (unit point charge) response of a passive cable model of a neurone with a branching dendritic geometry, soma and shunt:

$$v_r(x_r, z_e, t) = \sum_{n=0}^{\infty} E_n \psi_{en}(z_e/\lambda_e)\psi_{rn}(x_r/\lambda_r)e^{-t/\tau_n}, \qquad (56)$$

where the subscripts e and r refer to the input (excited) and recording segments, respectively, and z_e and x_r are the distances along the relevant segments of the stimulation and recording sites. The roots α_n of the recursive transcendental equation (Eqs. 19, 20, 22), together with Eq. 24, define the time constants τ_n. Equations 26 and 31 define the spatial eigenfunctions ψ_{jn}; the position-independent (Electrical) component E_n of each amplitude is given in Eq. 34; λ_j is the space constant of segment j (see List of Symbols).

TABLE 6 Naive estimates of τ_0 for two-cylinder + soma + shunt model

Waveform	τ_{eff_1} (20–30 ms)	τ_{eff_2} (40–50 ms)	$\tau_{eff_1}/\tau_{eff_2}$
$s \leftrightarrow s$	8.52	13.56	0.63
$1 \leftrightarrow s$	7.45	11.94	0.62
$2 \leftrightarrow s$	18.10	16.67	1.09
$1 \leftrightarrow 2$	20.25	16.84	1.20

* Apparent τ_0 [ms], estimated over given interval.

Waveform components

The solution does not allow the generation of any waveforms which cannot already be produced by means of compartmental models (although small soma, big shunt cases tend to require very small time steps). Indeed, compartmental models are far more flexible. The solution presented here, however, gives *direct access to the exponential components* of those waveforms produced by current inputs.

The time constants and amplitudes are useful in themselves, e.g., for (*a*) comparing different representations of the same cell, (*b*) understanding the parameter dependencies of responses (see below), (*c*) checking the accuracy of the *apparent* amplitudes and time constants extracted from waveforms by means of peeling (e.g, Ref. 13, p. 82) or exponential fitting, (*d*) assessing parameter estimation techniques which depend on the values of two or more time constants or amplitudes (or their ratios), e.g., the methods described in Refs. 3, 26, 29, 30, and 64, (*e*) comparing with the time constants and amplitudes obtainable from the eigenvalues and eigenvectors of matrices encoding compartmental models (e.g., Refs. 4, 25, 35).

Important aspects of the solution

(i) The most challenging part to implement is the search for the roots of the recursive transcendental equation (Eq. 22). These roots, α_n, give the time constants τ_n from Eq. 24.

(ii) These time constants are *independent* of stimulation and recording position: they hold for the entire cell.

(iii) The amplitudes A_n *are* affected by the stimulation and recording positions. One part E_n of each amplitude term is a constant over the entire cell, and depends only on the model parameters and the corresponding eigenvalue α_n. The second part ψ_{en} varies with the input (or excitation) site, and the third part ψ_{rn} varies with the recording position.

(iv) There is symmetry in the amplitudes between input and recording positions: interchanging them makes no difference to the waveform resulting from a particular stimulus. (This parallels the input-recording site symmetry in the

steady state solution.) See Paper II (36) for further discussion of this *reciprocity relation.*

Closely spaced time constants

Complicated geometries with many cylinders of differing electrotonic lengths produce many time constants within the range of interest (see Example 1, also Ref. 4). Sometimes these τ values are clustered. The vast majority of the associated amplitudes measured at the soma are relatively small. For complex geometries, particularly, it is extremely difficult to extract the time constants and amplitudes from the response waveforms (4) by peeling or by more sophisticated fitting techniques (e.g., Refs. 28, 71). This is because of the "severe nonorthogonality of exponentials" (28, 72): when the time constants are closely spaced, the contributions from neighboring components overlap with one another for most of their effective duration and thus cannot easily be separated.

Although imperfect, the various exponential extraction techniques can still convey an overall impression of the time constants and amplitudes in a waveform. It is probably easier and safer, however, to optimize model parameters by *directly* fitting model transients to target experimental waveforms (e.g., Refs. 20, 34, 45), rather than by attempting the extremely ill-conditioned two-stage process of first estimating the amplitudes and time constants of the experimental data and then matching the model's A and τ values to them. Direct fitting imposes model-specific constraints on the relative values of the time constants and amplitudes from the outset, rendering the overall process less sensitive to noise.

Intermediate charge redistribution components

Models with a shunt and two or more dendrites of unequal electrotonic lengths can generate large amplitude intermediate equalizing time constants (see Example 2). In such cases, when estimating the final time constant by linear regression on a semi-log plot, extremely late intervals should be used, to allow the earlier components to decay to negligible levels.

Care should be taken to ensure that experimental impulse responses or synaptic waveforms are not distorted by the effects of time-varying active conductances. It may be possible to eliminate voltage dependencies pharmacologically (e.g., Ref. 34). It should also be checked that the response scales linearly with the magnitude of the injected current. Noise may be a further problem if the waveform has decayed to small enough amplitudes. If sufficient precautions are not taken, and the regression interval is too early, the time constant may be seriously underestimated.

Parameter dependencies of impulse responses

The analytical solution gives considerable insight into the parameter dependence of voltage transients within complex branching cables. In all models, the amplitude terms are independent of R_m, and are inversely proportional to C_m. In models without a shunt, all the amplitude terms are also independent of R_i. Fast components of waveforms are independent of R_m and g_{shunt}; their amplitudes are always independent of R_i, and their time constants are proportional to R_i. All time constants are proportional to C_m. The amplitude terms of responses to other inputs are complicated by additional factors, but if the inputs are fast relative to the time constant concerned, the same general dependencies apply as for the impulse case. Early time solutions (Refs. 12, 2 (pp. 41–42)) also demonstrate the independence from R_m of the early parts of the responses.

Core models and raw parameter trade-offs

An n-segment *morphologically based* model has d_s and all the l_j and d_j values specified together with C_m, R_m, R_i, and g_{shunt}. This is a total of $2n + 5$ "*raw*" parameters (e.g, Table 4, top). The analytical solution shows that such models can be defined more compactly in terms of only $2n + 3$ "*core*" parameters,[3] namely, the set $\{\tau_m, g_s, \epsilon, g_{\infty_j}, L_j\}$, for all segments j (e.g., Table 4, middle). Reparameterization in terms of $\{\tau_m, g_{shunt}, g_{sm}, L_j, g_{\infty_j}\}$ allows g_{shunt} in the raw morphologically based specification to be carried through unchanged to the more compact core parameter set.

An infinite number of different possible raw morphologically based models yields the *same* core electrotonic model. All of these raw models therefore give *identical responses* to a particular input, providing stimulation and recording sites are at corresponding points on the different models[3] (27, 35). The raw parameters can trade off in many different ways (27), derivable from the definitions of the core parameters (see List of Symbols and Eq. 40). For a given core model, however, g_{shunt} must remain fixed. For example, suppose all lengths are increased by a factor F_l and all diameters by a factor F_d. The core model is preserved by making the following adjustments: R_i: $\times F_d^2/F_l$, R_m: $\times F_d F_l$, C_m: $\div F_d F_l$, g_{shunt}: no change, and d_s: $\times \sqrt{F_d F_l}$. Axial resistance, membrane conductance, and membrane capacitance are thereby conserved.

Core model nonuniqueness from fits to noisy data

In theory, fitting model responses to cell responses should allow the estimation of C_m, R_m, R_i and g_{shunt}, when combined morphological and electrophysiological data of sufficient quality are available from the *same* cell. In practice, when the target data is of poor quality (e.g., Fig. 3), core model nonuniqueness can be a problem: for a fixed morphology, many different combinations of electrical parameters (i.e., different core models) can yield indistinguishably good *fits*. When either input or recording site is changed from the fit configuration, the *predicted responses* of the competing models may differ dramatically (e.g., Ref. 20). This is potentially far

[3] J. D. Evans, G. C. Kember, and G. Major, manuscript submitted.

more serious than the uncertainty caused by the raw parameter trade-offs discussed above: at least in such cases the responses of the competing models are identical.

Exploring simplified representations

In many cases, it is desirable to simplify the morphology of neurones, both to make compartmental models of them run faster, and to give insights into the essential features of their electrical geometry (e.g., Refs. 4, 20, 35). The analytic solution will help in the further exploration of simplified representations such as the cartoon and double cylinder models presented above. Simplified representations also generate far fewer and more widely spaced α_n values, allowing much faster execution of the analytic solution (or compartmental model) programs.

Taper

It is useful to be able to make models with tapering dendrites, although the dendrites of many cells, including most of the visual cortical and hippocampal pyramidal cells measured in this laboratory (34, 73), show relatively little taper for most of their length. Analytic solutions exist for single tapering dendrites (e.g., Refs. 5, 27, 74, 75). Compartmental models can incorporate taper in a step-wise fashion to an arbitrary degree of accuracy (by using small enough compartments). This is also the approach advocated here for the analytic solution: tapering segments can be approximated as a chain of short cylinders of progressively smaller diameter.

Smooth input functions

If smooth current input functions composed of one or more exponential components are used, *lumped amplitude expressions* for the response component(s) with the input time constant(s) can be used to improve accuracy and speed (see Appendix 2). A lumped term can also be computed for part of the alpha function response. Similar expressions are used to calculate the steady-state voltage at late times following a current step (Appendix 3). If lumped terms are used, together with enough τ_n values, early artifacts due to missing components can practically be eliminated. The resulting waveforms are indistinguishable from comparable compartmental model output.

Problems

Ironically, most of the problems encountered have been with mathematically interesting but biologically implausible geometries (see Appendix 4). Special eigenvalues corresponding to roots of the transcendental equation (Eq. 22) "lost" in singularity clashes, and their associated amplitude terms, can largely be avoided by the measures described in Appendix 4. The subtle morphological adjustments required to avoid pairs of segments with an odd integer ratio of electrotonic lengths are small compared with realistic morphological measurement errors. The programs implementing the separation of variables solution behave robustly when the suggested default values are used for the neurones investigated so far (visual cortical, CA1 and CA3 pyramids, dentate gyrus granule cells, and substantia nigra cells).

Extensions to the model

The analytical solution can be generalized to models with nonuniform electrical parameters (where C_m, R_m, and R_i can vary from one segment to another, and where additional (steady) shunt conductances can be introduced at arbitrary locations in the dendritic tree). In addition, solutions have been obtained for the voltage clamp case (either voltage commands at the soma, or voltage-clamping synaptic currents). We hope to describe the nonuniform cases in future publications. The uniform parameter voltage clamp solution is presented in Paper II (36) of this series.

Comparison with other methods

The performance of the analytical solution programs has been compared to that of a compartmental modeling package which uses an *explicit* numerical integration scheme (14). There is extremely good agreement between the waveforms generated by the two techniques, when enough exponential components and compartments, respectively, are used.

The waveforms also agree well at early times with those generated by an implementation of Abbott's trip-based method (81) (G. Major, unpublished observations). Only models without a soma or shunt were compared.[4] Using a trip length cut-off of $5\sqrt{T}$, a 41-segment version of the cartoon model of the CA1 pyramid in Example 1, with the soma, shunt, and spine removed, required 22,500 trip terms by t = 3.4 ms, but gave good agreement up to that time. (Using a cut-off of only $4\sqrt{T}$ resulted in appreciable discrepancies from the correct solution.) The separation of variables solution required only 78 terms to achieve acceptable accuracy for times as early as 0.1 ms.

The analytic waveform generator runs approximately three times as fast as the compartmental modeling software when only one waveform is required, and the roots have to be found from scratch (although other, possibly more efficient, implementations of compartmental models are available (e.g., Refs. 15, 16, 44), and more detailed benchmarking could be carried out (76). Once the necessary eigenvalues of the analytic solution have been found; they can be stored, and

[4] Abbott's method can incorporate a soma implemented as a short cylinder. Its convergence properties deteriorate rapidly, however, when very short segments are included in a model, although in principle this could be dealt with by using time-varying weightings of the terms from trips touching such segments. As formulated, Abbott's trip-based solution does not cover models with shunts. The separation of variables solution handles soma, shunt, and short segments with no problems, but breaks down when extremely long segments are included (they produce many extremely closely spaced eigenvalues).

the calculation of waveforms resulting from different inputs into the same model is extremely rapid (approximately 50 times as fast as the compartmental model). By contrast, an entirely new compartmental model simulation must be run every time a different input is used, although waveforms from multiple recording sites can be generated simultaneously. If the recording site is the soma, as will be the case in most simulations, then the symmetry of the waveforms with respect to stimulation and recording sites can be exploited: one simulation with the input into the soma and recording from the various "input sites" would generate the same results as several simulations with the different input sites and somatic recording. (This applies to *current* but not to *conductance* inputs.) When composite inputs of several synaptic currents at different times and locations are desired, the compartmental model can incorporate all of these in one run, whereas the analytic solution would have to be used to calculate all of the responses individually before a separate program could add the waveforms (taking advantage of linearity).

The analytic solutions presented here cannot incorporate time-varying synaptic or active conductances: for these it is necessary to use compartmental models or time-stepping approximations incorporating the analytical solutions (e.g., following Refs. 24 and 77).

It is probably best to regard this analytic solution and its implementations as *complementary* to the established compartmental modeling packages, and Abbott's trip-based method. Each approach has different strengths and weaknesses. Using them in conjuction may allow some important new insights to be gained into the passive electrical properties of realistic dendritic trees.

SUMMARY AND CONCLUSIONS

1) A set of equations is used to define a passive cable model of a neurone with a soma and *shunt*, and one or more dendritic trees, each composed of *arbitrarily branching* cylindrical segments. A separation of variables solution in the form of a series of exponentially decaying components is derived for the voltage response following a point charge input. Input and recording sites can be anywhere on the soma or dendrites. The solution clarifies some of the parameter dependencies of the impulse response.

2) The eigenvalues of the solution, and hence the decay time constants, are given by the roots of a *recursive transcendental equation* obtained by applying the boundary conditions and the constraints of voltage continuity and current conservation. These time constants are determined by the whole model and are independent of input and recording positions. They are proportional to C_m, and faster components are also proportional to R_i and are independent of R_m and g_{shunt}.

3) The amplitudes of the components of the impulse response are obtained by means of a Laplace transform and complex residues. Each amplitude term can be expressed as the product of three factors, all dependent on the corresponding eigenvalue. The first is determined by the whole model and is the same over the entire soma-dendritic tree, the second varies with the input site, and the third varies with the recording position. The resulting amplitude term is symmetrical with respect to the input and recording sites, is inversely proportional to C_m, and is independent of R_m. The amplitudes of the faster components are also independent of shunt and R_i.

4) A reliable and efficient recursive root-finding algorithm is described for the transcendental equation. Lost roots arise when two or more singularities from different parts of the equation coincide, for example when the electrotonic lengths of "sister" terminal segments are odd integer ratios of one another. A new class of amplitude terms is required to complete the solution for these special cases. These additional amplitudes take non-zero values only within the subtrees involved in the singularity overlap; elsewhere they can be ignored. The appropriate expressions have been obtained for *nonbranching* subtrees, but not for singularity clashes between branching subtrees. Such singularity coincidences are rare and can be removed by small adjustments to the lengths of the involved segments. The usual amplitude expression then provides a very good approximation to the actual amplitude.

5) The responses to a number of common input functions are obtained analytically by convolution. The parameter dependencies of a given amplitude term are the same as for the impulse response, where the input is fast relative to its time constant. For currents composed of one or more exponentially decaying components, it is possible to derive lumped amplitude terms, using complex analysis, for all components of the response decaying with the input's time constant(s), thereby improving the accuracy of the solution. A similar lumped term can also be found for part of the response to alpha functions.

6) Complicated neuronal geometries can produce a large number of closely spaced time constants within the experimental range of interest. At the soma, many of their associated amplitudes are close to zero. This is illustrated with a 190-segment model of a CA1 pyramidal cell. Using far fewer terms, a simplified "cartoon" representation reproduces full model responses when stimulation and recording sites are not both in the same "collapsed" segment. When optimizing model parameters, direct fitting of experimental waveforms avoids the difficulties of extracting the exponential components.

7) Models with two or more dendrites of unequal electrotonic lengths and big shunts can produce large amplitude charge redistribution components with surprisingly slow time constants relative to the longest time constant (τ_0). These may dominate the waveform during regression intervals typically used experimentally for estimating τ_0, causing potentially serious underestimates of this measure. A simplified representation of a visual cortical pyramidal cell is used to illustrate this point.

8) The analytic solution described should be a useful complement to existing techniques, because it explicitly provides the time constants and amplitudes from which the response waveforms are composed. This information will be very helpful in further theoretical explorations of the effects of

dendrites of unequal electrotonic lengths and in comparisons of simplified representations. Implementations of the solution run about three times as fast as an existing compartmental modeling package when the eigenvalues have to be found from scratch, and about 50 times as fast when precomputed roots are used.

APPENDICES

Appendix 1: Derivation of amplitude terms using complex residues

Following Bluman and Tuckwell (31) and Evans et al. (10), it is shown below how to derive the Laplace transform of the impulse response for arbitrarily branching geometry with a soma + shunt. The purpose of this is 5-fold: (i) to demonstrate how the methods outlined in these papers can be generalized to the branching case by application of current conservation and voltage continuity constraints (following Ref. 38), (ii) to derive the amplitude terms A_n and E_n (Eqs. 33 and 34) by means of complex residues, (iii) to obtain lumped coefficients for terms containing e^{-at} or $e^{-t/\tau_{s_n}}$ in the responses to alpha functions or exponentially decaying inputs (see Appendix 2), (iv) to obtain D.C. and A.C. steady-state solutions (Appendix 3), (v) to obtain formulae for the coefficients $A_{n_{rr}}$ when there are singularity clashes at α_n (Appendix 4).

The essence of the complex residue technique is (i) to derive two different expressions for the Laplace transform of the desired response and (ii) to compare them to extract the amplitude coefficients.

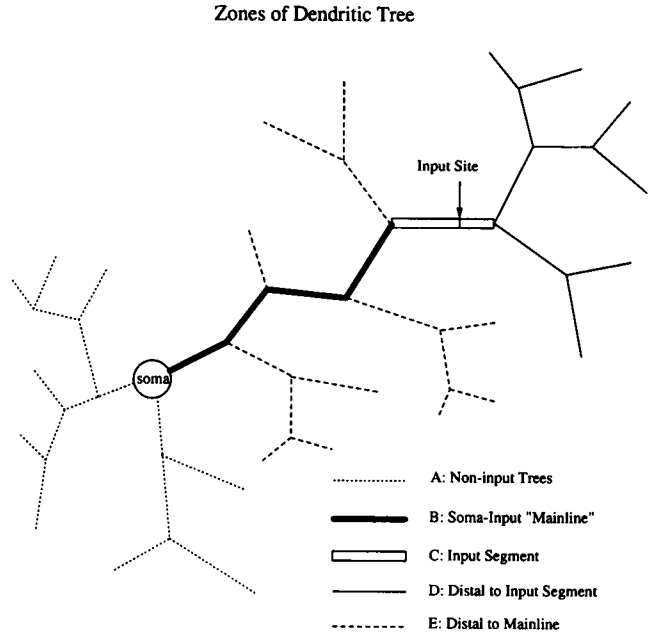

FIGURE 9 As part of the derivation in Appendix 1, the dendritic tree is divided up into five zones where the Laplace transform of the impulse response takes different forms, illustrated schematically here. *A*, noninput trees (Eq. 67); *B*, soma-input mainline (Eq. 68); *C*, input segment. Proximal (Eq. 68) and distal to input site (Eq. 70); *D*, segments distal to input segment (Eq. 70); *E*, segments distal to mainline (but not input) segments (Eq. 72).

Laplace transform of impulse response

Define $G_r(X_r, Z_e, t)$ to be the voltage response at X_r to a unit point charge at Z_e, (i.e., the same initial voltage condition as in Eq. 11). G_r is spatially continuous, including at branch points and at the soma (where it is defined to be G_s). Distances are in normalized units of λ_j, but times are in dimensional (standard S.I.) units.

The Laplace transform $\bar{G}_j(p)$ of $G_j(t)$ is defined, with respect to the complex variable p, to be

$$\bar{G}_j(p) = \int_0^\infty e^{-pt} G_j(t)\, dt. \tag{57}$$

It too is spatially continous.

The initial condition $G_j(t=0)$ is given in Equation 11. Taking Laplace transforms with respect to p of Eqs. 3, 4, 7, and 8, the ordinary differential \equation

$$\frac{d^2\bar{G}_j}{dX_j^2} - (\tau_m p + 1)\bar{G}_j = \begin{cases} -g_{\infty_e}^{-1}\delta(X_e - Z_e) & \text{if } j = e \quad (a), \\ 0 & \text{otherwise} \quad (b), \end{cases} \tag{58}$$

is obtained, with the following boundary conditions.

(i) At termininations,

$$\left(\frac{d\bar{G}_j}{dX_j}\right)_{X_j = L_j} = 0, \tag{59}$$

(ii) at branches,

$$g_{\infty_p}\left(\frac{d\bar{G}_p}{dX_p}\right)_{X_p = L_p} = \sum_{d \in dtrs_p} g_{\infty_d}\left(\frac{d\bar{G}_d}{dX_d}\right)_{X_d = 0}, \tag{60}$$

and (iii) at the soma,

$$g_s\bar{G}_s(1 + \epsilon\tau_m p) = g_s\bar{G}_s[1 + \epsilon(q^2 - 1)] = \sum_{st \in stems} g_{\infty_{st}}\left(\frac{d\bar{G}_{st}}{dX_{st}}\right)_{X_{st} = 0}, \tag{61}$$

defining

$$q \equiv \sqrt{1 + \tau_m p}. \tag{62}$$

Integrating Eq. 58a with respect to X_e between Z_e^- and Z_e^+, just either side of the input site, gives another *boundary* condition (in the Laplace domain) from the original *initial* condition (in the time domain):

$$\lim_{Z_e^+ \to Z_e} \frac{d\bar{G}_e}{dX_e} - \lim_{Z_e^- \to Z_e} \frac{d\bar{G}_e}{dX_e} = -g_{\infty_e}^{-1}. \tag{63}$$

Let $\mathcal{P}(j)$ be the parent of segment j.

Define

$$\bar{\mu}_p = \frac{1}{g_{\infty_p}} \sum_{d \in dtrs_p} g_{\infty_d}\left(\frac{1 + \bar{\mu}_d \coth qL_d}{\coth qL_d + \bar{\mu}_d}\right) \tag{64}$$

and

$$\bar{\mu}_j = 0 \quad \text{for all terminal segments } j, \tag{65}$$

used below to enforce the boundary conditions (Eqs. 59 and 60), and

$$\bar{\kappa}_j = \prod_{c \in chain_j} (\cosh qL_c + \bar{\mu}_c \sinh qL_c)^{-1}, \tag{66}$$

used to ensure continuity of $\bar{G}_j$ (e.g., see Eq. 67).

The derivation of $\bar{\mu}_j$ and $\bar{\kappa}_j$ is similar to that of μ_j and κ_{jn} in the main part of this paper and mirrors the working in Ref. 38.

Dividing the dendritic tree into five zones, illustrated in Fig. 9, a convenient solution to Eq. 58, which implicitly incorporates continuity and the termination and branch boundary conditions, is:

(*a*) Segments in noninput trees:

$$\bar{G}_j = \bar{\kappa}_j\bar{A}_s[\cosh q(L_j - X_j) + \bar{\mu}_j \sinh q(L_j - X_j)], \tag{67}$$

where $\bar{A}_s$ is a constant to be determined.

(*b*) Segments on "mainline" chain from soma to input segment ($\forall c \in chain_e$): Starting from the stem segment and moving distally toward the

input segment, an extra term is added to Eq. 67 every time a branch point is crossed into the next chain segment c. These terms are to represent the effect of the input, i.e., boundary condition (Eq. 63). They must be zero at the proximal end of the segment in which they are introduced, to ensure continuity of $\bar{G}_c$. A convenient form is sinh qX_c:

$$\bar{G}_c = \bar{\kappa}_c(\bar{A}_c[\cosh q(L_c - X_c) + \bar{\mu}_c \sinh q(L_c - X_c)] + \bar{B}_c \sinh qX_c), \quad (68)$$

where, for a parent p and daughter c on the chain,

$$\bar{A}_c = \bar{A}_p + \bar{B}_p \sinh qL_p \quad (69)$$

and for the chain's stem segment st, $\bar{A}_{st} = \bar{A}_s$, to ensure continuity of $\bar{G}$ at branch points and the soma, respectively. The $\bar{B}_c$ values are constants to be determined.

In this way, the problem has been separated implicitly into two parts, the branch/terminal boundary conditions and the input boundary condition, represented by different parts of the solution.

(c) Input segment itself: (i) proximal to input site ($X_e \leq Z_e$), $\bar{G}_e$ is given by Eq. 68, (ii) distal to input site ($X_e \geq Z_e$), $\bar{G}_e$ is given by Eq. 70.

(d) Segments in subtree distal to input segment:

$$\bar{G}_j = \bar{\kappa}_j \bar{C}[\cosh q(L_j - X_j) + \bar{\mu}_j \sinh q(L_j - X_j)]. \quad (70)$$

Equating the right hand sides of Eqs. 68 and 70 at Z_e gives

$$\bar{C} = \bar{A}_e + \frac{\bar{B}_e \sinh qZ_e}{[\cosh q(L_e - Z_e) + \bar{\mu}_e \sinh q(L_e - Z_e)]}. \quad (71)$$

(e) Other segments in subtrees distal to a mainline (type b) segment:

$$\bar{G}_j = \bar{\kappa}_j \bar{A}_c[\cosh q(L_j - X_j) + \bar{\mu}_j \sinh q(L_j - X_j)], \quad (72)$$

where c is the most proximal on-chain segment which is *not* an "ancestor" of j, i.e. $\bar{A}_c$ is taken from the most distal on-chain branch point on the path between the soma and segment j.

Determination of $\bar{A}_c$ *and* $\bar{B}_c$ values.

Substituting Eqs. 68 and 70 into the new boundary condition (Eq. 63) at the input site gives

$$(\bar{C} - \bar{A}_e)[\sinh q(L_e - Z_e) + \bar{\mu}_e \cosh q(L_e - Z_e)] + \bar{B}_e \cosh qZ_e = \frac{1}{\bar{\kappa}_e q g_{\infty_e}}. \quad (73)$$

Substituting Eq. 71 into Eq. 73 and simplifying, gives

$$\bar{B}_e = \frac{[\cosh q(L_e - Z_e) + \bar{\mu}_e \sinh q(L_e - Z_e)]}{\bar{\kappa}_{\mathcal{P}(e)} q g_{\infty_e}}, \quad (74)$$

where $\mathcal{P}(e)$ is the parent segment of e. (If e is a stem segment, then $\bar{\kappa}_{\mathcal{P}(e)} = 1$.)

A recursive relation is now required between $\bar{B}_p$ and $\bar{B}_c$, for a parent segment p and daughter segment c on the soma-input chain. Since Eq. 60 holds at the branch point between them, it follows that

$$g_{\infty_p} \bar{\kappa}_p[\bar{B}_p \cosh qL_p - \bar{A}_p \bar{\mu}_p] = \bar{\kappa}_c g_{\infty_c} \bar{B}_c - \bar{A}_c \sum_{d \in dtrs_p} g_{\infty_d} \bar{\kappa}_d[\sinh qL_d + \bar{\mu}_d \cosh qL_d]. \quad (75)$$

Substitution of Eq. 69 into Eq. 75, and cancellation of the $\bar{A}_p$ terms, using the definition of $\bar{\mu}_p$ (Eq. 64) and $\bar{\kappa}_p/\bar{\kappa}_c$ from Eq. 66, gives

$$\bar{B}_p = \frac{g_{\infty_c}}{g_{\infty_p}} \frac{\bar{B}_c}{(\cosh qL_p + \bar{\mu}_p \sinh qL_p)(\cosh qL_c + \bar{\mu}_c \sinh qL_c)}. \quad (76)$$

Starting from Eq. 74 and using Eq. 76 to work back toward the chain's stem segment st, it follows that

$$\bar{B}_{st} = \frac{\bar{\kappa}_e[\cosh q(L_e - Z_e) + \bar{\mu}_e \sinh q(L_e - Z_e)]}{\bar{\kappa}_{st} q g_{\infty_{st}}}. \quad (77)$$

From the somatic boundary condition (Eq. 61) and from Eq. 77 it can be shown that

$$\bar{A}_s = \frac{\bar{\kappa}_e[\cosh q(L_e - Z_e) + \bar{\mu}_e \sinh q(L_e - Z_e)]}{g_s[1 + \epsilon(q^2 - 1)] + q \sum_{st \in stems} g_{\infty_{st}} \dfrac{(\sinh qL_{st} + \bar{\mu}_{st} \cosh qL_{st})}{(\cosh qL_{st} + \bar{\mu}_{st} \sinh qL_{st})}}. \quad (78)$$

Equations 67–72, 74, 76, and 78 can be used to evaluate $\bar{G}_r(X_r, Z_e, p)$ over the entire dendritic tree.

Obtaining $A_{n_{er}}$ *by complex residues*

Following Refs. 10 and 31, in cases where there are no singularity coincidences in the transcendental function (Eq. 53), the Laplace transform of

$$G_r(X_r, Z_e, t) = \sum_{n=0}^{\infty} A_{n_{er}} e^{-t/\tau_n} \quad (79)$$

can also be written as

$$\bar{G}_r(X_r, Z_e, p) = \sum_{n=0}^{\infty} \frac{A_{n_{er}}}{(p + 1/\tau_n)}. \quad (80)$$

It can be seen that $A_{n_{er}}$ is the coefficient of $(p + 1/\tau_n)^{-1}$, which in complex variable theory is called the *residue* of $\bar{G}_r(X_r, Z_e, p)$ at $p = -1/\tau_n$, i.e., at $q = i\alpha_n$.

Let

$$h(p) = q^{-1} \bar{\kappa}_e \bar{\kappa}_r[\cosh q(L_e - Z_e) + \bar{\mu}_e \sinh q(L_e - Z_e)] \times [\cosh q(L_r - X_r) + \bar{\mu}_r \sinh q(L_r - X_r)] \quad (81)$$

and

$$k(p) = g_s[1 + \epsilon(q^2 - 1)]q^{-1} + \sum_{st \in stems} g_{\infty_{st}} \frac{(\sinh qL_{st} + \bar{\mu}_{st} \cosh qL_{st})}{(\cosh qL_{st} + \bar{\mu}_{st} \sinh qL_{st})}. \quad (82)$$

From both Eqs. 78 and 80, it can be seen that $\bar{G}_r(X_r, Z_e, p)$ has simple poles at $p = -1/\tau_n$, in the former case by comparing $k(p)$ with the transcendental function (Eq. 53). Thus, providing there are no singularity clashes, near one of these poles the $\bar{A}_s$ term comes to dominate $\bar{G}_r(X_r, Z_e, p)$ irrespective of stimulating or recording position. By standard methods of complex analysis (Ref. 78, p. 110), evaluating the residues of $\bar{G}_r(X_r, Z_e, p)$,

$$A_{n_{er}} = \lim_{p \to -1/\tau_n} (p + 1/\tau_n)\bar{G}_r(X_r, Z_e, p) = \frac{h(p)}{\dfrac{dk(p)}{dp}} = \frac{h(p)}{\left(\dfrac{dk(p)}{dq}\right)\left(\dfrac{dq}{dp}\right)}. \quad (83)$$

From Eq. 62, $dq/dp = \tau_m/2q$, so

$$\frac{dk(p)}{dp} = \frac{\tau_m}{2q}\left\{ g_s[\epsilon + (\epsilon - 1)q^{-2}] + \sum_{st \in stems} \frac{g_{\infty_{st}}}{(\cosh qL_{st} + \bar{\mu}_{st} \sinh qL_{st})^2} \times \left[\left(L_{st}(\cosh qL_{st} + \bar{\mu}_{st} \sinh qL_{st}) + \frac{d\bar{\mu}_{st}}{dq} \cosh qL_{st} \right) \times (\cosh qL_{st} + \bar{\mu}_{st} \sinh qL_{st}) - \left(L_{st}(\sinh qL_{st} + \bar{\mu}_{st} \cosh qL_{st}) + \frac{d\bar{\mu}_{st}}{dq} \sinh qL_{st} \right) \times (\sinh qL_{st} + \bar{\mu}_{st} \cosh qL_{st}) \right] \right\}. \quad (84)$$

The terms in the *square brackets* on the last two lines simplify to

$$\left[L_{st}(1-\bar{\mu}_{st}^2)+\left\langle\frac{d\bar{\mu}_{st}}{dq}\right\rangle\right], \tag{85}$$

where $\langle\square\rangle$ is used to indicate terms that can be expanded recursively. Similarly, it can be shown that

$$\frac{d\bar{\mu}_p}{dq}=\frac{1}{g_{\infty_p}}\sum_{d\in dtrs_p} g_{\infty_d}\frac{\left[L_d(1-\bar{\mu}_d^2)+\left\langle\frac{d\bar{\mu}_d}{dq}\right\rangle\right]}{(\cosh qL_d+\bar{\mu}_d\sinh qL_d)^2}. \tag{86}$$

Starting from Eq. 84, recursively expanding terms marked by $\langle\square\rangle$ using Eq. 86 and the definition of $\bar{\mu}_p$ (Eq. 64) until the tip segments are reached (bearing in mind the definition of $\bar{\kappa}_j$ (Eq. 66)), it can be shown that

$$\frac{dk(p)}{dp}=\frac{\tau_m}{2q}\left\{g_s\left[2\epsilon-(1+\epsilon(q^2-1))q^{-2}\right]+\sum_{j\in segs} g_{\infty_j}\bar{\kappa}_j^2L_j(1-\bar{\mu}_j^2)\right\}. \tag{87}$$

To obtain the amplitude terms $A_{n_{er}}$ (Eq. 33) and $E_{n_{er}}$ (Eq. 34) given in the main part of the paper, take Eqs. 83, 81, and 87 and make the following substitutions (which hold from the definitions of the relevant quantities):

$$\begin{aligned}&q=i\alpha_n,\\&\cosh i\alpha_n=\cos\alpha_n\\&\sinh i\alpha_n=i\sin\alpha_n,\\&\bar{\mu}_j(i\alpha_n)=-i\mu_{jn},\\&\bar{\kappa}_j(i\alpha_n)=\kappa_{jn}.\end{aligned} \tag{88}$$

Appendix 2: Lumped terms with smooth input functions

Artifacts

Unfortunately, the waveforms resulting from convolving smooth, relatively slow input currents with the impulse response suffer from artifacts lasting roughly five times the maximum input current time constant, if this is much slower than the fastest τ_n used. This is because only a finite number of terms with the input time constant can be included in the computed transient, while excluding a large number of terms with the same time constant but only slowly diminishing amplitudes. For example, in the case of the exponentially decaying synaptic current (Eq. 49), if N is the index of the fastest cell time constant, and if $\tau_N \ll \tau_{sy}$, then the artifact will be approximately

$$\left(\sum_{n=N+1}^{\infty}\frac{QA_{n_{er}}}{(\tau_{sy}/\tau_n-1)}\right)e^{-t/\tau_{sy}}. \tag{89}$$

If τ_n is only slowly converging, and there is no particular trend in the $A_{n_{er}}$ values, the artifact could be quite considerable.

Following Appendix 4 of Ref. 31, it is shown below, using calculus of residues, how to obtain closed form expressions incorporating *all* of the terms decaying with the input time constants. This is most convenient for exponentially decaying inputs, although the method can also be applied to alpha function inputs.

Single exponentially decaying current

All terms containing $e^{-t/\tau_{sy}}$ in Eq. 50 can be lumped together:

$$V_r(X_r,Z_e,t)=H_{er}e^{-t/\tau_{sy}}+\sum_{n=0}^{\infty}\frac{QA_{n_{er}}}{(1-\tau_{sy}/\tau_n)}e^{-t/\tau_n}. \tag{90}$$

H_{er} is equal to the expression in *large parentheses* in Eq. 89, with the summation starting from $n = 0$.

The Laplace transform of Eq. 90 is

$$\bar{V}_r(X_r,Z_e,p)=\frac{H_{er}}{(p+1/\tau_{sy})}+\sum_{n=0}^{\infty}\frac{QA_{n_{er}}}{(1-\tau_{sy}/\tau_n)(p+1/\tau_n)}. \tag{91}$$

The Laplace transform of the voltage response can also be written as the product of the Laplace transforms of the input function (Eq. 49) and the impulse response:

$$\bar{V}_r(X_r,Z_e,p)=\frac{Q\bar{G}_r(X_r,Z_e,p)}{\tau_{sy}(p+1/\tau_{sy})}. \tag{92}$$

Both Eqs. 91 and 92 have simple poles at $p=-1/\tau_{sy}$ (i.e. $q=\sqrt{1-\tau_m/\tau_{sy}}$), so it follows that

$$H_{er}=\lim_{p\to -1/\tau_{sy}}\frac{Q\bar{G}_r(X_r,Z_e,p)}{\tau_{sy}}. \tag{93}$$

Where $\tau_{sy} > \tau_m$, q is real and $\bar{G}_r(X_r, Z_e, p)$ can be evaluated using Eqs. 64–72, 74, 76 and 78. However, in many cases, $\tau_{sy} < \tau_m$, so q is complex, and we let $q = iw$, where $w=\sqrt{\tau_m/\tau_{sy}-1}$. Special cases occur when τ_{sy} is equal to one of the τ_n values. Substitutions (Eq. 88) must then be used in these equations, with w instead of α_n, together with $\bar{A}_j(iw)=A_j'(w)$ and $\bar{B}_j(iw)=-iB_j'(w)$ to obtain appropriate recursive expressions for evaluating $\bar{G}$ (the prime ′ does not imply differentiation here):

(*a*) Noninput trees:

$$\bar{G}_j=\kappa_jA_s'[\cos w(L_j-X_j)+\mu_j\sin w(L_j-X_j)], \tag{94}$$

where μ_j and κ_j are defined in Eq. 19 and 28, respectively, but dropping subscripts n and with $\alpha = w$,

$$A_s'=\frac{\kappa_e[\cos w(L_e-Z_e)+\mu_e\sin w(L_e-Z_e)]}{g_s[1-\epsilon(w^2+1)]-w\sum_{st\in stems}g_{\infty_{st}}\frac{(1-\mu_{st}\cot wL_{st})}{(\cot wL_{st}+\mu_{st})}}. \tag{95}$$

(*b*) Soma-input mainline:

$$\bar{G}_c=\kappa_c(A_c'[\cos w(L_c-X_c)+\mu_c\sin w(L_c-X_c)]+B_c'\sin wX_c), \tag{96}$$

where, at the chain's stem segment st, $A_{st}'=A_s'$, and for a parent p and daughter c on the chain,

$$A_c'=A_p'+B_p'\sin wL_p \tag{97}$$

and

$$B_p'=\frac{g_{\infty_c}}{g_{\infty_p}}\frac{B_c'}{(\cos wL_p+\mu_p\sin wL_p)(\cos wL_c+\mu_c\sin wL_c)}. \tag{98}$$

(*c*) Input segment itself: (i) if $X_e \le Z_e$, use Eq. 96, (ii) if $X_e > Z_e$, use Eq. 100, with

$$B_e'=\frac{[\cos w(L_e-Z_e)+\mu_e\sin w(L_e-Z_e)]}{\kappa_{\mathcal{P}(e)}wg_{\infty_e}}, \tag{99}$$

where $\mathcal{P}(e)$ is segment e's parent.

(*d*) Distal to input:

$$\bar{G}_j=\kappa_jC'[\cos w(L_j-X_j)+\mu_j\sin w(L_j-X_j)]. \tag{100}$$

$$C'=A_e'+\frac{B_e'\sin wZ_e}{[\cos w(L_e-Z_e)+\mu_e\sin w(L_e-Z_e)]}. \tag{101}$$

(e) Others distal to soma-input mainline:

$$\bar{G}_j = \kappa_j A'_c[\cos w(L_j - X_j) + \mu_j \sin w(L_j - X_j)], \quad (102)$$

where c is the most proximal on-chain segment which is *not* an ancestor of j.

Double exponential current

By a similar derivation, the amplitudes of the lumped terms corresponding to the sums of the second and third terms in Eq. 52, with time constants τ_{sy_1} and τ_{sy_2}, respectively, are

$$\frac{(Q\bar{G}_r(X_r, Z_e, p = -1/\tau_{sy_1})}{\tau_{sy_1} - \tau_{sy_2}} \quad (103)$$

and

$$\frac{Q\bar{G}_r(X_r, Z_e, p = -1/\tau_{sy_2})}{\tau_{sy_2} - \tau_{sy_1}}. \quad (104)$$

Alpha function current

Lumping terms as in Ref. 31, Appendix 4, the voltage response (Eq. 48) to an alpha function current (Eq. 47) is

$$V_r(X_r, Z_e, t) = H_{er}te^{-at} + J_{er}e^{-at} + \sum_{n=0}^{\infty} \frac{Qa^2A_{n_{er}}}{(1/\tau_n - a)^2} e^{-t/\tau_n}. \quad (105)$$

The Laplace transform of this response can be written either as

$$\bar{V}_r(X_r, Z_e, p) = \frac{Qa^2\bar{G}_r(X_r, Z_e, p)}{(p + a)^2} \quad (106)$$

or as

$$\bar{V}_r(X_r, Z_e, p) = \frac{H_{er}}{(p + a)^2} + \frac{J_{er}}{(p + a)} + \sum_{n=0}^{\infty} \frac{Qa^2A_{n_{er}}}{(1/\tau_n - a)^2(p + 1/\tau_n)}. \quad (107)$$

Both expressions have a pole of order two at $p = -a$, giving us

$$H_{er} = \lim_{p \to -a} Qa^2\bar{G}_r(X_r, Z_e, p). \quad (108)$$

J_{er} is the complex residue of $\bar{V}_r(X_r, Z_e, p)$ (i.e the coefficient of the term in $(p + a)^{-1}$). This is given by (Ref. 78, p. 110)

$$J_{er} = \lim_{p \to -a} Qa^2 (d\bar{G}_r(X_r, Z_e, p)/dp). \quad (109)$$

In principle this can be evaluated, but complicated branching geometries generate ugly, recursive differentials. In practice, because coefficients of the terms of the form e^{-at} in Eq. 48 have $(1/\tau_n - a)^2$ in the denominator, when sufficient terms are included to ensure that $1/\tau_n \gg a$, the artifacts due to missing terms can be made negligible. A hybrid implementation, with the lumped $H_{er}te^{-at}$ term and unlumped $\sum_{n=0}^{N} - (Qa^2A_{n_{er}}/(1/\tau_n - a)^2)\, e^{-at}$ terms has proved satisfactory in all cases tested ($a \geq 0.01\ ms^{-1}$).

Appendix 3: Steady-state

Steady-state solution

Setting $p = 0$ in Eqs. 58–63, gives the system of equations describing a unit steady-state current input into one branch. (This observation has been made in a number of previous studies.) The steady-state solution $\hat{v}_r(x_r, z_e)$ is therefore obtained by setting $p = 0$ (and thus $q = 1$) in Eqs. 64–72, 74, 76 78. If the injected current is i_{in}, then

$$\hat{v}_r(x_r, z_e) = i_{in}\bar{G}_r(X_r, Z_e, p = 0) = i_{in}R_{er}. \quad (110)$$

$R_{er} = \bar{G}_r(X_r, Z_e, p = 0)$ is the steady-state transfer resistance between the stimulation and recording sites. Setting $r = e$ and $X_r = Z_e$ gives the input resistance at a given point, which may be compared with the results in Refs. 23 and 38.

Efficacy and attenuation

The relative efficacy of an input can be defined as V_{es}/V_{ss} where V_{es} is the voltage at the soma resulting from a given dendritic input into segment e, and V_{ss} is the voltage at the soma for the same input into the soma. Because of the symmetry of the solution with respect to input and recording sites, this is equal to the steady-state voltage clamp efficacy V_{se}/V_{ss}, where V_{se} is the voltage at the dendritic location resulting from the same input into the soma. The steady-state efficacy of an input at distance Z_e along segment e is given by

$$\begin{aligned}\text{Eff}(Z_e) &= \bar{G}_{st}(X_{st} = 0, Z_e, p = 0)/\bar{G}_{st}(X_{st} = 0, Z_{st} = 0, p = 0) \\ &= \bar{\kappa}_e[\cosh(L_e - Z_e) + \bar{\mu}_e \sinh(L_e - Z_e)], \end{aligned} \quad (111)$$

with $q = 1$ in the $\bar{\mu}$ and $\bar{\kappa}$ terms defined in Eqs. 64 and 66, where st is any stem segment. This measure does not depend on g_{shunt}. Let V_{ee} be the voltage at the dendritic site following an input there. The steady-state attenuation, defined as steady V_{ee}/V_{es} can be calculated from $\bar{G}_e(Z_e, Z_e, p = 0)/\bar{G}_{st}(X_{st} = 0, Z_e, p = 0)$. Unlike efficacy, this measure *does* depend on the shunt. See Appendix 3 of Paper II (36) for a discussion of A.C. attenuation.

Appendix 4: Singularity clashes

Lost roots at coinciding singularities

The relative positions of singularities along the α axis can be changed by adjusting the physical dimensions of selected segments of the model cell. Some adjustments can cause neighboring singularities to approach one another. As two or more singularities tend to the same value of α, the intervening root will be "trapped" between them and will vanish. Consider the simple two-dendrite case without soma or shunt. Let K, M, and N be any fixed positive (or zero) integers. As $(2M + 1)L_1 \to (2N + 1)L_2$, the singularities at $\alpha = (2K + 1)(2N + 1)\pi/2L_1$ and $\alpha = (2K + 1)(2M + 1)\pi/2L_2$ can become arbitrarily close, until the root between them is "lost", when the electrotonic lengths are exactly in an odd number ratio. From Eqs. 33 and 31, it can be seen that the eigenvalues corresponding to these lost roots produce zero-amplitude components at the soma, since $\mu_{jn} = 0$ for terminal segments, and if $\alpha_n L_j = (2K + 1)(2N + 1)\pi/2$, then $\cos \alpha_n L_j = 0$. However, this is not the case in the particular dendrites responsible for the coinciding singularities. Simulations with compartmental models have confirmed that these missed components are necessary, since, without them, the analytic solution produces a different waveform to the equivalent compartmental model. When $L_1 = L_2$, the analytic solution output is the same as that of a compartmental model with the two dendrites *collapsed together* into an equivalent cylinder. Changing one of the offending L values by a small amount (e.g., 1 in 10^6) can resurrect the lost roots: as long as the singularities are separated by a finite interval, however small, there will necessarily be a zero-crossing between them. There is virtually no change in the compartmental model output after such a trivial morphological change, but the analytic solution now gives the same waveform as the uncollapsed case.

A detailed discussion of these special cases is given in Ref. 10. Essentially, they are caused by the existence of a second class of eigenfunctions of the form of Eq. 26, but with $\kappa_{jn} = 1$, corresponding to eigenvalues at singularity coincidences. In the same paper, expressions are derived for the amplitudes associated with these eigenfunctions for the multicylinder unbranched geometry. Similar expressions apply to terminal segments in the branched case:

$$A_{n_{er}} = -\left(\frac{2\psi_{en}(Z_e)\psi_{rn}(X_r)}{\tau_m L_e L_r(\sin \alpha_n L_e \sin \alpha_n L_r)}\right)\left[\sum_{j \in involved} \frac{g_{\infty_j}}{L_j}\right]^{-1}, \quad (112)$$

where $e \neq r$, and where *involved* refers to the set of all segments contributing to the coinciding singularities. When $e = r$,

$$A_{n_{er}} = \frac{2\psi_{en}(Z_e)\psi_{en}(X_e)}{\tau_m L_e^2}\left(\left[\frac{g_{\infty_e}}{L_e}\right]^{-1} - \left[\sum_{j\in involved}\frac{g_{\infty_j}}{L_j}\right]^{-1}\right). \quad (113)$$

Each eigenfunction is zero at the parent branch point of the subtrees involved in its particular singularity coincidence, and at all points outside the involved subtrees. However, within those subtrees involved in the coincidence, the eigenfunction has different associated amplitudes according to whether input and recording sites are in the same or different subtrees. At the parent branch point, the sum over all the involved subtrees of the axial currents contributed by all the extra eigenfunctions is zero. In other words, the rest of the dendritic tree cannot "sense" these eigenfunctions, and they make no contributions to voltages or currents outside the subtrees in which they are generated.

It is useful to remark that the existence of these odd (zero at parent branch) subtree eigenfunctions is inherent in Rinzel and Rall's superposition method of solution (79, 80) and is responsible for the values of their B_m and B_k (Ref. 80, pp. 767–768) being zero when the point of observation is proximal to the input branch. The higher order time constants (for equalization between sister branches or subtrees) are associated with non-zero coefficients only when the point of observation is in the same subtree as the input branch: they note that this accounts for the differences found in computing the transients of their Fig. 3.

In principle, following the complex analysis methods outlined in Appendix 1, it is possible to derive expressions for the amplitude terms for any recording or stimulating position and combination of singularity clashes. However, in practice, since there are arbitrarily many potential combinations of singularity clashes between segments of different generations and subtrees, this route seems quite unattractive for the general case. Perhaps expressions for particular regular geometries could be derived in the future, if this seemed useful.

Measures to prevent coincidence of singularities

Unfortunately, models with a symmetrical structure, which may be of interest to theoreticians, do suffer from singularity coincidences. Because of the difficulty of deriving amplitudes for the special eigenfunctions in the case of branching geometry, and because of the extra "accounting" involved in keeping track of particularly awkward cases, such as singularity coincidences between subtrees at different depths, the following computational strategy has been adopted:

1) The programs allow the option of adding the same small increment (e.g., 0.001 μm) to each physical length as it is read in. This partly compensates for the user rounding off the physical measurements entered into the input file, thereby unwittingly increasing the chances of odd integer ratios of lengths. The small increment reduces such occurrences where the diameters of two segments with nominally equal L values are different, or where the diameters are the same, but the physical lengths are in an odd integer ratio other than 1:1.

2) The dendritic tree can be screened for subtrees from a common branch point which are within a user-specified fraction (default 10^{-6}) of being odd-integer ratios of one another in terms of their component L values. The programs only screen for ratios which would lead to a singularity coincidence at an α less than that corresponding to the fastest time constant of interest. When such cases occur, small increments can be added to the L values of one subtree. The process is repeated for the whole dendritic tree until no odd-integer ratios remain.

3) The root-finder defines a singularity coincidence to have occurred whenever two or more singularities are found separated by less than a certain interval $TOL/L_{\mathrm{eff}_{max}}$, where TOL is a small number, e.g., 10^{-10}. The periods of the tangent functions composing the transcendental function (Eq. 53) are scaled along the α axis by $1/L_j$, so the criterion is scaled by a similar factor, the maximum effective electrotonic length over all the segments, where L_{eff_p} is defined recursively for segment p with daughters d by

$$L_{\mathrm{eff}_p} = L_p + \frac{1}{g_{\infty_p}}\sum_{d\in dtrs_p} g_{\infty_d} L_{\mathrm{eff}_d}. \quad (114)$$

The root-finder tags the coincidence with the indices of the most proximal segments of the involved subtrees. In really unpleasant cases, there may be more than one group of these for a given singularity coincidence, and conceivably these could originate from different generations of subtrees. This information, along with the final list of eigenvalues, is displayed by the waveform generator after the root-finding stage is completed.

At this point, unless the offending segments are terminations, for which special amplitude expressions (Eqs. 112 and 113) have been derived, it is best to abandon the simulation, make adjustments to the relevent parts of the dendritic morphology, and start again. This step is unnecessary if there are to be no simulations involving simultaneous input into and recording from the involved subtrees.

The transients that are produced by the waveform generator after trivial morphological adjustments cannot be distinguished from the original compartmental model output. As long as the computer has sufficient precision, this ad hoc numerical means of evading the special cases seems a robust way of solving the problem of coinciding singularities.

In practice, the lost roots problem can be solved in the way described for very complex dendritic trees, e.g., for hippocampal CA1 pyramidal cells with around 200 segments, by making length adjustments (of the order of 1 in 10^6) that are orders of magnitude smaller than the likely measurement errors (10–20%).

G. Major is currently a Wellcome Mathematical Biology Training Fellow and was formerly a Wellcome Prize Student. J. D. Evans has been funded by a Science and Engineering Research Council CASE award and from a Wellcome Trust program grant. We would like to thank the Wellcome Trust for funding the SUN computer system, John Clements and Steve Redman for the use of a compartmental modeling package, Guy Kember, Alan Larkman, Ken Stratford, and James Sneyd for helpful discussions, and the referees of a previous incarnation of this paper for constructive criticism.

REFERENCES

1. Hounsgaard, J., and J. Midtgaard. 1989. Dendrite processing in more ways than one. *Trends Neurosci.* 12:313–315.
2. Jack, J. J. B., D. Noble, and R. W. Tsien. 1975. Electric Current Flow in Excitable Cells. Oxford: Oxford University Press, Oxford, UK. 502 pp.
3. Rall, W. 1969. Time constants and electrotonic length of membrane cylinders and neurons. *Biophys. J.* 9:1483–1508.
4. Holmes, W. R., I. Segev, and W. Rall. 1992. Interpretation of time constant and electrotonic length estimates in multicylinder or branched neuronal structures. *J. Neurophysiol.* 68:1401–1420.
5. Jack, J. J. B. 1979. An introduction to linear cable theory. *In* The Neurosciences: Fourth Study Program. F. O. Schmitt, and F. G. Worden, editors. M. I. T. Press, Cambridge, MA. 423–437.
6. Gustafsson, B., and M. J. Pinter. 1984. Relations among passive electrical properties of lumbar alpha-motoneurones of the cat. *J. Physiol.* 356:401–431.
7. Iansek, R., and S. J. Redman. 1973. The amplitude, time course and charge of unitary excitatory post-synaptic potentials evoked in spinal motoneurone dendrites. *J. Physiol.* 234:665–688.
8. Edwards, F. A., A. Konnerth, B. Sakmann, and T. Takahashi. 1989. A thin slice preparation for patch clamp recordings from neurones of the mammalian central nervous system. *Pflügers Arch.* 414:600–612.
9. Jackson, M. B. 1992. Cable analysis with the whole-cell patch clamp. Theory and experiment. *Biophys. J.* 61:756–766.
10. Evans, J. D., G. C. Kember, and G. Major. 1992. Techniques for obtaining analytical solutions to the multi-cylinder somatic shunt cable model for passive neurones. *Biophys. J.* 63:350–365.
11. Abbott, L. F., E. Fahri, and S. Gutmann. 1991. The path integral for dendritic trees. *Biol. Cybern.* 66:49–60.
12. Abbott, L. F. 1992. Simple diagrammatic rules for solving dendritic

cable problems. *Physica A.* 185:343–356.

13. Rall, W. 1977. Core conductor theory and cable properties of neurons. *In* Handbook of Physiology. The Nervous System. Cellular Biology of Neurones. E. R. Kandel, editor. Am. Physiol. Soc., Bethesda, MD. Sect. 1, Vol. 1, Part 1. 39–98.
14. Clements, J. D. 1984. Ph.D. dissertation. Expt. Neurology Unit, John Curtin School of Medical Research, Australian National University, Canberra.
15. Hines, M. 1984. Efficient computation of branched nerve equations. *Int. J. Biomed. Comput.* 15:69–76.
16. Hines, M. 1989. A program for simulation of nerve equations with branching geometries. *Int. J. Biomed. Comput.* 24:55–68.
17. Segev, I., J. W. Fleshman, J. P. Miller, and B. Bunow. 1985. Modeling the electrical properties of anatomically complex neurons using a network analysis program: passive membrane. *Biol. Cybern.* 53:27–40.
18. Mascagni, M. V. 1989. Numerical methods for neuronal modeling. *In* Methods in Neuronal Modelling. C. Koch, and I. Segev, editors. M. I. T. Press, Cambridge, MA. 439–484.
19. Mascagni, M. V. 1991. A parallelizing algorithm for computing solutions to arbitrarily branched cable neuron models. *J. Neurosci. Meth.* 36:105–114.
20. Stratford, K. J., A. J. R. Mason, A. U. Larkman, G. Major, and J. J. B. Jack. 1989. The modeling of pyramidal neurones in the visual cortex. *In* The Computing Neurone. R. Durbin, C. Miall, and G. Mitchison, editors. Addison-Wesley, Reading, UK. 296–321.
21. Butz, E. G., and J. D. Cowan. 1974. Transient potentials in dendritic systems of arbitrary geometry. *Biophys. J.* 14:661–689.
22. Turner, D. A. 1984. Segmental cable evaluation of somatic transients in hippocampal neurons (CA1, CA3, and Dentate). *Biophys. J.* 46:73–84.
23. Koch, C., and T. Poggio. 1985. A simple algorithm for solving the cable equation in dendritic trees of arbitrary geometry. *J. Neurosci. Meth.* 12:303–315.
24. Holmes, W. R. 1986. A continuous cable method for determining the transient potential in passive dendritic trees of known geometry. *Biol. Cybern.* 55:115–124.
25. Perkel, D. H., B. Mulloney, and R. W. Budelli. 1981. Quantitative methods for predicting neuronal behaviour. *Neuroscience.* 6:823–837.
26. Holmes, W. R., and W. Rall. 1992. Electrotonic length estimates in neurons with dendritic tapering or somatic shunt. *J. Neurophysiol.* 68: 1421–1437.
27. Holmes, W. R., and W. Rall. 1992. Estimating the electrotonic structure of neurons with compartmental models. *J. Neurophysiol.* 68:1438–1452.
28. Provencher, S. W. 1976. A Fourier method for the analysis of exponential decay curves. *Biophys. J.* 16:26–41.
29. Durand, D. 1984. The somatic shunt cable model for neurons. *Biophys. J.* 46:645–653.
30. Kawato, M. 1984. Cable properties of a neuron model with non-uniform membrane resistivity. *J. Theor. Biol.* 111:149–169.
31. Bluman, G. W., and H. C. Tuckwell. 1987. Techniques for obtaining analytical solutions for Rall's model neuron. *J. Neurosci. Meth.* 20: 151–166.
32. Churchill, R. V. 1942. Expansions in series of non-orthogonal functions. *Am. Math. Soc. Bull.* 48:143–149.
33. Major, G., A. U. Larkman, and J. J. B. Jack. 1990. Constraining non-uniqueness in passive electrical models of cortical pyramidal neurones. *J. Physiol.* 430:23P.
34. Major, G. 1992. The physiology, morphology and modeling of cortical pyramidal neurones. D.Phil. thesis. Laboratory of Physiology, Oxford University. 275 pp.
35. Rall, W., R. E. Burke, W. R. Holmes, J. J. B. Jack, S. J. Redman, and I. Segev. 1992. Matching dendritic neuron models to experimental data. *Physiol. Rev.* 72:S159–S186.
36. Major, G., J. D. Evans, and J. J. B. Jack. 1993. Solutions for transients in arbitrarily branching cables: II. Voltage clamp theory. *Biophys. J.* 65:450–468.
37. Major, G. 1993. Solutions for transients in arbitrarily branching cables: III. Voltage clamp problems. *Biophys. J.* 65:469–491.
38. Rall, W. 1959. Branching dendritic trees and motoneuron membrane resistivity. *Exp. Neurol.* 1:491–527.
39. Poznanski, R. R. 1987. Techniques for obtaining analytical solutions for the somatic shunt cable model. *Math. Biosci.* 83:1–23.
40. Rall, W. 1967. Distinguishing theoretical synaptic potentials computed for different soma-dendritic distributions of synaptic input. *J. Neurophysiol.* 30:1138–1168.
41. Jack, J. J. B., and S. J. Redman. 1971. The propagation of transient potentials in some linear cable structures. *J. Physiol.* 215:283–320.
42. Tuckwell, H. C. 1988. Introduction to Theoretical Neurobiology. Vol. 1. Linear Cable Theory and Dendritic Structure. Cambridge University Press, Cambridge, UK. 291 pp.
43. Colquhoun, D., P. Jonas, and B. Sakmann. 1992. Action of brief pulses of glutamate on AMPA/kainate receptors in patches from different neurones of rat hippocampal slices. *J. Physiol.* 458:261–287.
44. Wilson, M. A., and J. M. Bower. 1989. The simulation of large-scale neural networks. *In* Methods in Neuronal Modelling. C. Koch, and I. Segev, editors. M. I. T. Press, Cambridge, MA. 291–333.
45. Clements, J. D., and S. J. Redman. 1989. Cable properties of cat spinal motoneurons measured by combining voltage clamp, current clamp and intracellular staining. *J. Physiol.* 409:63–87.
46. Nelder, J. A., and R. Mead. 1965. A geometric technique for optimisation. *Computer J.* 7:308–327.
47. Press, W. H., B. P. Flannery, S. A. Teukolsky, and W. T. Vetterling. 1988. Numerical Recipes in C: The Art of Scientific Computing. Cambridge University Press, Cambridge, UK. 735 pp.
48. Harris, K. M., and J. K. Stevens. 1989. Dendritic spines of CA1 pyramidal cells in the rat hippocampus: serial electron microscopy with reference to their biophysical characteristics. *J. Neurosci.* 9:2982–2997.
49. Jack, J. J. B., A. U. Larkman, G. Major, A. J. R. Mason, and K. J. Stratford. 1989. Simplified representations and compartmental modeling of cortical pyramidal neurones. *J. Physiol.* 417:3P.
50. Benz, R., O. Frölich, P. Läuger, and M. Montal. 1975. Electrical capacity of black lipid films and of lipid bilayers made from monolayers. *Biochim. Biophys. Acta.* 394:323–334.
51. Fettiplace, R., D. M. Andrews, and D. A. Haydon. 1971. The thickness, composition and structure of some lipid bilayers and natural membranes. *J. Membr. Biol.* 5:277–296.
52. Fricke, H. 1931. The electrical conductivity and capacity of disperse systems. *Physics.* 1:106–115.
53. Schwan, H. P., and E. L. Carstensen. 1957. Dielectric properties of the membrane of lysed erythrocytes. *Science.* 15:985–986.
54. Takashima, S., and H. P. Schwan. 1974. Passive electrical properties of squid axon membrane. *J. Membr. Biol.* 17:51–68.
55. Takashima, S. 1976. Membrane capacity of squid giant axon during hyper- and depolarisations. *J. Membr. Biol.* 27:21–39.
56. Haydon, D. A., J. Requena, and B. W. Urban. 1980. Some effects of aliphatic hydrocarbons on the electrical capacity and ionic currents of the squid giant axon membrane. *J. Physiol.* 309:229–245.
57. Larkman, A. U., G. Major, K. J. Stratford, and J. J. B. Jack. 1992. Dendritic morphology of pyramidal neurones of the visual cortex of the rat: IV. Electrical geometry. *J. Comp. Neurol.* 323:153–166.
58. Larkman A., K. Stratford, and J. Jack. 1991. Quantal analysis of excitatory synaptic action and depression in hippocampal slices. *Nature.* 350:344–347.
59. Larkman, A., and A. Mason. 1990. Correlations between morphology and electrophysiology of pyramidal neurons in slices of rat visual cortex. I. Establishment of cell classes. *J. Neurosci.* 10:1407–1414.
60. Peters, A., and I. R. Kaiserman-Abramof. 1970. The small pyramidal neuron of the rat cerebral cortex. The perikaryon, dendrites and spines. *Am. J. Anat.* 127:321–356.
61. Larkman, A. U. 1991. Dendritic morphology of pyramidal neurones of the visual cortex of the rat: III. Spine distributions. *J. Comp. Neurol.* 306:332–343.
62. Spain, W. J., P. C. Schwindt, and W. E. Crill. 1987. Anomalous rectification in neurons from cat sensorimotor cortex in vitro. *J. Neurophysiol.* 57:1555–1576.
63. Rose, P. K., and A. Dagum. 1988. Nonequivalent cylinder models of neurons: interpretation of voltage transients generated by somatic current injection. *J. Neurophysiol.* 60:125–148.
64. Brown, T. H., D. H. Perkel, J. C. Norris, and J. H. Peacock. 1981.

Electrotonic structure and specific membrane properties of mouse dorsal root ganglion neurons. *J. Neurophysiol.* 45:1–15.

65. Gnam, W. 1987. The two time constant model of the neurone. M.Sc. thesis, Oxford University. 78 pp.
66. Segev, I., and W. Rall. 1983. Theoretical analysis of neuron models with dendrites of unequal electrotonic lengths. *Soc. Neurosci. Abstr.* 9:102. 20, p. 341.
67. Holmes, W. R., and W. Rall. 1987. Estimating the electrotonic structure of neurons which cannot be approximated as equivalent cylinders. *Soc. Neurosci. Abstr.* 13:422.7, p. 1517.
68. Turner, D. A. 1988. Waveform and amplitude characteristics of evoked responses to dendritic stimulation of CA1 guinea-pig pyramidal cells. *J. Physiol.* 395:419–439.
69. Nitzan, R., I. Segev, and Y. Yarom. 1990. Voltage behavior along the irregular dendritic structure of morphologically and physiologically characterised vagal motoneurons in the guinea pig. *J. Neurophysiol.* 63:333–346.
70. Moore, J. A., and K. Appenteng. 1991. The morphology and electrical geometry of rat jaw-elevator motoneurones. *J. Physiol.* 440:325–343.
71. Yeramian, E., and P. Claverie. 1987. Analysis of multiexponential functions without a hypothesis as to the number of components. *Nature.* 326:169–174.
72. Lanczos, C. 1988. Applied Regression Analysis. Dover, New York. 272–280.
73. Larkman, A. U. 1991. Dendritic morphology of pyramidal neurones of the visual cortex of the rat: I. Branching patterns. *J. Comp. Neurol.* 306:307–319.
74. Strain, G. M., and W. D. Brockman. 1975. A modified cable model for neuron processes with non-constant diameters. *J. Theor. Biol.* 51:475–494.
75. Poznanski, R. R. 1991. A generalized tapering equivalent cable model for dendritic neurones. *Bull. Math. Biol.* 53:457–467.
76. Bhalla, U. S., D. H. Bilitch, and J. M. Bower. 1992. Rallpacks: a set of benchmarks for neuronal simulators. *Trends Neurosci.* 15:453–458.
77. Wilson, C. J. 1984. Passive cable properties of dendritic spines and spiny neurons. *J. Neurosci.* 4:281–297.
78. Priestley, H. A. 1985. Introduction to Complex Analysis. Oxford University Press, Oxford, UK. Chapter 7.
79. Rall, W., and J. Rinzel. 1973. Branch input resistance and steady attenuation for input to one branch of a dendritic model neuron. *Biophys. J.* 13:648–688.
80. Rinzel, J., and W. Rall. 1974. Transient response in a dendritic neuron model for current injected at one branch. *Biophys. J.* 14:759–790.
81. Cao, B. J., and L. F. Abbott. 1993. A new computational method for cable theory problems. *Biophys. J.* 64:303–313.
82. White, J. A., P. B. Manis, and E. D. Young. 1992. The parameter identification problem for the somatic shunt model. *Biol. Cybern.* 66: 307–318.